Ophthalmic Application of Optical Coherence Tomography Based Angiography for Choroidal Imaging

Zhongdi Chu

A thesis

submitted in partial fulfillment of the

requirements for the degree of

Master of Science in Bioengineering

University of Washington

2015

Committee:

Ruikang Wang

Tueng Shen

Program Authorized to Offer Degree:

Department of Bioengineering

University of Washington

Abstract

Ophthalmic Application of Optical Coherence Tomography and Optical Coherence Tomography Angiography on Choroidal in vivo Imaging

Zhongdi Chu

Chair of the Supervisory Committee:

Dr. Ruikang Wang

Bioengineering

Choroid is a vascular layer composed predominantly of blood vessels, highly pigmented melanocytes, nerves and connective tissue. It lays between the sclera and retinal pigment epithelium (RPE) and provides oxygen and nutrients to the outer retina as well as RPE. For the avascular fovea region, choroid is the sole source for metabolic exchange. Choroidal circulation accounts for 85% of the whole ocular circulation and the blood flow ranges from 800 to 2000 mL/min/100 g of tissue. The malfunction of choroidal circulation is closely associated with several ocular diseases such as age-related macular degeneration (AMD), diabetic retinopathy (DR), central serous chorioretinopathy (CSC) and so on. Choriocapillaris is the first vascular layer in choroid and closest to retina. The inflammation of choriocapillaris is connected with malfunction and loss of RPE as well as choroidal neovascularization, whose pathological process is still not completely understood. Choroidal circulation also plays an essential role in ocular thermoregulation and eye volume maintenance. It's mainly achieved by adjusting the thickness of

choroid. The subfoveal choroidal thickness (SFCT) also increase as the severity worsened from nonproliferative diabetic retinopathy (NPDR) to proliferative diabetic retinopathy (PDR) and that highly myopic eyes' choroidal thickness are statistically significantly thinner than non-myopic age matched eyes and choroidal thickness is related to vision acuity. Therefore, in this thesis, an improved method for choroid thickness has been developed and validated. To the best of author's knowledge, the choriocapillaris visualization demonstrated in this thesis is the first time choriocapillaris have been imaged by spectral domain OCT with complex signal approach at a large field of view.

Contents

List of tables

List of figures

Chapter 1

Chapter 2

Choriocapillaris visualization with complex signal based OCT Angiography - OMAG

Abstract

We demonstrated *in vivo* choriocapillaris imaging in normal human subjects with a Cirrus HD 5000 spectral domain OCT prototype. With the tracking system installed in the prototype and the montage scanning protocol, wide field OCT angiograms of 9 mm * 11 mm were created. OCT angiography utilizes the intrinsic motion of red blood cells as contrast mechanism therefore requires no exogenous contrast agents as fluorescein angiography and indocyanine green angiography do. Four consecutive OCT scans were acquired at the same location for angiography generating, intensity based, phase based and complex signal based OCTA were all computed and compared. With the ability to resolve fine and detailed vascular lobules, complex signal based OMAG were selected for *en face* visualization. In consistency with histological studies, lobular vascular networks were observed and corresponding feeding arterioles were identified in OMAG images. Structural OCT *en face* image was also generated and at periphery regions, lobular structures can also be recognized with distinct brightness patterns. This study showcased the feasibility of using commercialized SD-OCT for *in vivo* choriocapillaris visualization and essentially opens the possibility for clinical imaging studies on choriocapillaris' role in pathogenesis and early diagnosis of ocular disease.

Introduction

Choroid, locates at the posterior part of uvea between sclera and retinal pigmented epithelium (RPE), is a thin layer composed predominantly of blood vessels, highly pigmented melanocytes, nerves and connective tissues. As a key component to maintain the normal vision, choroid not only provides blood flow and nutrients to the outer retina including photoreceptors, but also is solely responsible for the metabolic exchange for the avascular retinal fovea. Choroidal circulation also plays an essential role in ocular thermoregulation and eye volume maintenance [1-3]. As a highly vascular layer as choroid is, its blood circulation constitutes 85% of the whole eye and ranges from 800 to 2000 mL/min/100 g of tissue [4]. Naturally, the malfunction of choroidal circulation is associated with several ocular diseases such as age-related macular degeneration (AMD), diabetic retinopathy (DR), central serous chorioretinopathy (CSC) and so on. As the most adjacent to retina choroidal vascular layer, choriocapillaris is a thin but dense planar capillary bed composed of polygonal vascular units that are called lobules. Many postmortem histological efforts have been put into choriocapillaris visualization and scanning electron microscope (SEM) has also been utilized for ex vivo imaging [5-10]. The feeding arterioles from deeper choroid insert into the choriocapillaris plane perpendicularly with round open connecting points and the draining venues are orientated circumferentially around the lobules, which are filled and drained independently. Studies [11-13] show that the dysfunction, atrophy or absence of choriocapillaris are associated -with the loss of retinal pigment epithelium (RPE) in GA cases. Moreover, any form of choriocapillaris loss may stimulate drusen formation, resulting in the death of photoreceptors in AMD [14, 15]. The consequential resorption of drusen and the loss of the RPE (hypopigmentation) can be used to anticipate the development and progression of geographic atrophy. Bhutto *et. al* reported that the

mutualistic symbiotic relationship between the RPE, photoreceptors, the Bruch's membrane and the choriocapillaris was found to be lost not only in atrophic AMD but in wet AMD cases too [16]. In neovascular AMD [17], it was observed that choriocapillaris loss usually occurs with an intact RPE, which can be due to blood supply reduction from large vessel stenosis, or from the development of toxic milieu in the choriocapillaris. The death of the choriocapillaris affects the neighboring RPE, causing hypoxia. The resulting hypoxic RPE can lead to new vessel formation from the choriocapillaris, leading to choroidal neovascularization (CNV). Gartner *et. al* [18] also reported the absence of RPE and choriocapillaris in retinis pigmentosa (RP) with histological studies. Moreover, studies [19, 20] on diabetic retinopathy (DR) have shown that the vessel density of choriocapillaris are smaller in DR patients compared to normal subjects. Thus, in vivo high resolution visualization of the structure and blood flow of choriocapillaris could be very essential for the better understanding of the disease pathosphysiology and would potentially play an important role in early diagnosis of ocular diseases, treatment monitoring, patients management and so on.

The in vivo imaging of choriocapillaris is mainly limited by the highly pigmented nature of choroid and the fact that it's located under RPE. Fluorescein angiography (FA) and indocyanine green angiography (ICGA) have both been used for in vivo imaging [21-23] but the fenestrated nature of choriocapillaris leads to dye leakage which makes high resolution imaging of choriocapillaris problematic and challenging. Therefore, FA and ICGA have been mainly used for choroidal perfusion pattern investigation and time measurement.

Optical Coherence Tomography (OCT) is a recently developed optical imaging technology that utilize the back-scattered photons to visualize depth-resolved 3D structures in biological tissues. [24-27] OCT has gained massive acceptance in ophthalmology clinics for cross-sectional

structure visualization in the posterior eye. OCT-based angiography (OCTA) is a newly introduced tool for in vivo 3D vasculature imaging without usages for exogenous contrast agents and it is also gaining acceptance among clinicians for its applications in retinal and choroidal imaging. Optical micro-angiography (OMAG) as one algorithm of OCTA has been introduced and utilized for vascular network imaging in the past few years for various applications [28-30] and its complex signal based nature is especially suitable for contrasting capillaries with slow flow velocity such as choriocapillaris. Previous studies of choroidal OCT applications have been mainly focused on choroidal thickness measurement [31-35] or choroidal vasculature [36-38] with the absence of RPE. To the best our knowledge, there are only a few studies that have been using OCT for choriocapillaris imaging up to date. For studies utilizing phase information, Kurokawa et al. demonstrated choriocapillaris imaging in normal subjects with adaptive optics OCT in the macular region with limited field of view and speed [39]; Braaf et al. installed a second scanning laser ophthalmoscope as hardware tracking system and demonstrated choriocapillaris imaging under the fovea for a normal subject [40], also limited field of view and imaging speed. For other studies utilizing intensity information of OCT signal, Choi et al. used speckle decorrelation to contrast choriocapillaris and choroidal large vessels with a home built 400 kHz swept source OCT (SSOCT) system, which is unrealistic for commercial use in the near future and also limited by its field of view and low sensitivity for slow flow rate blood vessels [41]. Up to date, in vivo studies on choriocapillaris are of very limited numbers and the pathological roles of choriocapillaris in ocular diseases progression remain relatively unexplored and unknown, future investigated and study are essential for the better understanding of choriocapillaris in normal and pathological eyes.

In this study, we investigate in vivo choriocapillaris imaging using a Cirrus HD 5000 spectral domain OCT prototype (Carl Zeiss Meditec Inc., Dublin, CA, USA) with 68 kHz A-line acquisition speed 842 nm central wavelength. The simple yet elegant complex signal based

OMAG algorithm enables the visualization of choriocapillaris with high sensitivity and specificity, combined with the tracking system and montage scanning protocol, large field of view imaging of choriocapillaris is achieved for normal subjects consistent with histological findings.

Materials and Methods

OCT System and Scanning Protocols

The OCT system used in this study is a Cirrus HD 5000 spectral domain OCT system (Carl Zeiss Meditec Inc., Dublin, CA, USA), the A-line acquisition speed is 68 kHz and the central wavelength is 842 nm. The scanning protocol provides a field of view of 2.4×2.4 mm^2 with 245 lines in the fast scan direction (B-mode) and 245 frames in the slow scan axis. With the tracking system turning on, a customized size montage scan can be acquired with 10% overlay between each cubes, thus achieving a large field of view with post scan image stitching. In this study, we acquired a 9 mm * 11 mm field of view with 20 cubes for two normal subjects centered at fovea and optic nerve head respectively. For each subject, scanning was performed in a dark room without their pupil dilated. In order for OMAG to contrast the moving red blood cells (RBCs), 4 B-scans were acquired repeatedly at same location, with 245 A-lines a frame for 245 B frames, one cube scan takes ~3.5 s. Subjects could take rests during different cube scans as they wish, the relative position of different cubes are recorded by the tracking system thus enable the montage stitching.

Choriocapillaris Angiography

In this study, we used a complex signal based approach – OMAG for blood vessel network contrasting in choriocapillaris. To obtain the complex signal, fast Fourier transform was performed on the dispersion-compensated k-space spectral data. Then bulk motion between B-scans was detected and removed with a block matching method using cross-correlation. After

bulk motion correction, a phase compensation algorithm was implemented and the signal pre-processing was finished.

The way OMAG works is that it essential reflects the motion of red blood cells in vascular networks. When RBCs travel along the blood vessels, photons will interact with RBCs and either scatter backward or forward as a result. During this process, the velocity of the photons will change as the direction changes, thus introducing the Doppler shift and phase change of the light wave. As a result, in our detected signals, there will be a phase difference in the 4 repeated B-scans where RBC is passing through. The intensity difference among those four B frames is more straightforward as the RBC is moving constantly during the acquisition process thus the number of photons interact with RBC will change so the intensity will be different for those 4 repeated scans.

As showed in Figure 1, for each voxel in 3D OCT data, the signal comes from the summation of photons backscattered in the focal spot. The static tissue signal could be represented as the dark blue vector in the complex coordinates, this is the signal we have from the first B-scan of the four B frames cluster. Assuming there is movement in this voxel, after a certain time interval, the second B frame will be obtained, and the OCT signal from the second scan is represented as the light blue dashed vectors. Therefore, the movement between those two scans can be represented as the earthy yellow vectors. The detectable movement range can be represented as the dark blue circle. It should be noted that the range would not be a perfect ring as the sensitivity of intensity differences and phase differences are different and it would also vary from different OCT systems, but for the purpose of simple illustration, it's exemplified as a circle.

As presented in Figure 2, those detectable movement vectors could be categorized into different case scenarios. First is showed in Figure 2(b), the complex difference, intensity difference and phase difference has been illustrated as yellow, purple and green arrow respectively, in this case, all three approaches can detect the motion signal. However, the complex approach will have

maximum signal strength, as compared to intensity, the triangle inequality decides that the complex signal strength will always be larger than intensity signal strength and the phase difference is just a component of the complex difference. Second case scenario is showed in Figure 2(c), there is movement between those two frames but there is no change in amplitude in the signal, thus the movement signal can only be detected by complex approach and phase approach, the complex signal strength would still be larger than phase signal for the same reason explained in (b). For the last case as showed in Figure 2(d), there is no phase difference but intensity difference between these two frames, thus only intensity and complex approach are useful. However, on thing should be noted in this situation is that in reality, this case where there is no phase change doesn't exist. Because that as long as there is movement in the signal, the Doppler shift will introduce phase change to the signal, the plausible situation for Figure 2 (b) is that the phase change is exactly 2π and the detected value is 0. For times when the phase difference falls under the noise floor and cannot be detected, Figure 2 (b) would apply and complex signal strength would still be larger than intensity signal.

To clarify furthermore, the OCT signal at first scan capture can be written as $A_1 e^{-i\varphi_1}$, the OCT signal at second scan capture can be written as $A_2 e^{-i\varphi_2}$. The OCTA result of complex approach can be written as:

$$\begin{aligned} &\left| A_1 e^{-i\varphi_1} - A_2 e^{-i\varphi_2} \right| \\ &= \sqrt{\left(A_1 e^{-i\varphi_1} - A_2 e^{-i\varphi_2} \right)^2} \\ &= \sqrt{A_1^{\,2} + A_2^{\,2} - 2A_1 A_2 \cos\left(\Delta\varphi\right)} \end{aligned} \tag{1}$$

When Normalize the OMAG signal to the structural OCT signal, the OCTA results can be written as:

$$\begin{aligned}
&\sqrt{\frac{A_1^2 + A_2^2 - 2A_1A_2 + 2A_1A_2 - 2A_1A_2\cos(\Delta\varphi)}{(A_1^2 + A_2^2)}} \\
&= \sqrt{\frac{(A_1 - A_2)^2 + 2A_1A_2 - 2A_1A_2\cos(\Delta\varphi)}{(A_1^2 + A_2^2)}} \\
&= \sqrt{\frac{(A_1 - A_2)^2 + 2A_1A_2(1 - \cos(\Delta\varphi))}{(A_1^2 + A_2^2)}} \\
&\sqrt{\frac{(A_1 - A_2)^2}{(A_1^2 + A_2^2)} + \frac{A_1A_2}{(\frac{A_1^2 + A_2^2}{2})}(1 - \cos(\Delta\varphi))}
\end{aligned} \tag{2}$$

Where essentially, $\frac{(A_1 - A_2)^2}{(A_1^2 + A_2^2)}$ represents the speckle variance approach as one of the intensity approaches and $\frac{A_1A_2}{(\frac{A_1^2 + A_2^2}{2})}(1 - \cos(\Delta\varphi))$ represents the amplitude decorrelations modulated by phase differences. Therefore, the signal of complex OMAG takes both the intensity variance and complex decorrelation into consideration and essentially exploit all possible the motion contrast mechanism in OCT signals. In conclusion, either the phase OCTA approach or the intensity OCTA approach can only detect part of the whole motion signal and essentially throw away useful information. Therefore, for the purpose of obtaining the entirety of the motion signal as much as possible, complex OCTA approach – OMAG was used in this study. OMAG takes the differences of those 4 consecutive scans by simply subtracting complex signals from repeated B-scans at same location:

$$F_{OMAG}(x,z) = \frac{\frac{1}{R-1}\sum_{n=1}^{R-1}\left|I_{n+1}(x,z) - I_n(x,z)\right| + \sqrt[3]{\prod_{n=1}^{R-1}\left|I_{n+1}(x,z) - I_n(x,z)\right|}}{2} \tag{3}$$

Where I is the complex, intensity or phase OCT signal, R is the number of repeated B-scans at same location, n is the index of repeated B-scans and x, z correspond to the pixel coordinates in a signal B-scan. As dense as choriocapillaris are, signal to noise ratio (SNR) is crucial for vascular network visualizing for a better contrast between moving RBCs and static tissues. The arithmetic mean and geometric mean were both calculated and averaged in order to furtherly boost SNR, for the reason that the noise pattern calculated by these two means would be different whereas the signal would be similar. As illustrated in Figure 3, the differences of the 4 B-scans was taken and showed in Figure 3. (b)-2, as a thin layer as choriocapillaris is, segmentation is crucial for the visualization. RPE was delineated in the structure image (Figure 3. (b)-1) and the same segmentation was applied on the blood flow image (Figure 3. (b)-2).

Results and Discussion

In the Cirrus system we used in this study, 1024 pixels on one A-line correspond to ~3 mm of tissue in air, the pixel size is ~2.2 μm in tissue. There are 245 A-lines per B frame and 245 B frames correspond to 2.4 mm in air, thus the pixel size on transversal plane is ~ 7.3 μm in tissue. The lateral resolution of this system is ~ 15 μm and the axial resolution is ~ 7.5 μm, so we have approximately 2 times oversampling rate on the transversal plane and 3 times oversampling on the axial direction to ensure the visualization of choriocapillaris. Choriocapillaris is a thin layer of 10-20 μm in depth, therefore corresponded number of pixels was taken below the Bruch's membrane for *en face* visualization as showed in Figure 4. Figure 4 (a) – (d) show the visualization of choriocapillaris slab with different thickness. Our results agree with the histological findings on choriocapillaris thickness measurement. 11 μm thick choroidal slabs 20 μm under Bruch's membrane (Figure 4 (e)) and 11 μm thick choroidal slabs 30 μm under Bruch's membrane (Figure 4 (f)) are showed for visualization of deeper bigger choroidal vessels. Contrary to retinal big vessels, deep choroidal vessel appear to be dark on OCT and OCTA images. Our hypothesis is that this phenomenon is due to the low backscattering of choroidal moving signals.

As the g factor of blood is ~ 0.998, only a small part of photons scatter back from choroidal blood vessels and few of those can manage travel back to interfere with reference arm lights, most of those photons are blocked by RPE, therefore giving a dark representation of deeper choroidal vessels.

As indicated in equation (3), both the arithmetic mean (AM) and geometric mean (GM) are calculated and average to boost the SNR and achieve a better contrast for choriocapillaris vascular imaging. Figure 5 shows the comparison of AM mean approach and AM+GM approach. Figure 5 (a)-(d) are the structure, intensity flow, complex flow and phase flow images of AM approach and (e)-(h) are the same *en face* images for AM+GM approach. The phase images show the most evident SNR improvement as the phase differences are generally susceptible to noises and fluctuates more than intensity signals. Pointed by red arrows, the AM+GM approach demonstrates a better contrast for visualizing the radial blood vessel patterns and better contrast in general.

Figure 6 shows the *en face* OCT and OCT angiography imaging of choriocapillaris with three different approaches –OMAG intensity ((b), (e)), OMAG phase ((c), (f)) and OMAG complex ((d), (h)). Figure 6(a)-(d) are linear display and (e)-(h) are log display. As illustrated in Figure 1 and Figure 2, the intensity approach and phase approach both only use part of the OCT signal therefore lose the entirety of OCT angiography. In accordance with our theory, our result proves that OMAG, the complex signal based OCTA is superior to intensity and phase signal based OCTA in visualizing choriocapillaris. As it can be observed in Figure 5, the intensity signal based OCTA is highly dependent on the strength of structure signal, it lose the ability to differentiate moving tissue from static tissue almost completely when the structure signal is small, as indicated by the yellow arrow. However, both phase signal based OCTA and complex signal based OCTA are capable of resolving the motion signal where the OCT signal is relatively low. Another note can be made on the result comparison is that the phase based OCTA is heavily influenced by the

notorious tailing artifacts. Pointed by the red arrows, the tails of retinal blood vessels are very evident in the phase based OCTA approach. This is because that the tailing artifacts is mainly introduced by the forward scattering photons. When photons travel through retinal vessel, they interact with erythrocytes, instead of bouncing back, they scatter forth and continue to travel to deeper tissues and scatter back at later interaction with tissues. In this process, the phase of the light is changed due to Doppler shift, but little intensity variation is introduced by the first interaction. Accordingly, the retinal vessel appear to be dark on the structure and intensity OCTA image in (a) and (b) due to the absorption and appear to be bright on the phase OCTA image in (c) because of the Doppler shift introduced by strong forward scattering. On the other hand, there is no obvious tailing artifact in linear displayed complex signal based OMAG, which is another reason why OMAG is superior for choriocapillaris visualization.

As described before, the tracking system was installed in this prototype to enable large field of view montage scan. 20 cubes of 2.4 mm*2.4mm each was stitched together to achieve a large field image of 9 mm * 11mm. To the best of our knowledge, this is the first time that choriocapillaris has been imaged and examined at this large a scale by commercialized spectral domain OCT. As presented in Figure 7, the characteristic of choriocapillaris at different locations can be clearly visualized with complex OMAG linear display. Consistent with findings reported by histological studies, choriocapillaris under the macular region are denser and have smaller vessel diameters. Confined by the lateral resolution of OCT, they appear to be a densely packed honeycomb vascular network. When moving away from fovea towards the equator and periphery, the lobular structure of choriocapillaris can be recognized more clearly as the vessels become less dense and vessel diameters become larger. Figure 8 – 10 are the intensity OCTA, phase OCTA and structure OCT *en face* images of the exactly same data set with exactly same segmentation. It can be concluded that the complex OMAG provides more detail information on the lobular vascular network visualization and better connectivity among capillaries. The phase OCTA is

suitable for contrasting capillaries with slow flow but lose lots of information since it throws away intensity contrast. Moreover, as the phase information is highly polluted by the forward scattering photons from retinal vessels, the phase OCTA is immensely contaminated by the tailing artifacts. The intensity OCTA preserves the brightness contrast of structure OCT, but it lacks the ability to perceive the finer details of choriocapillaris because of throwing away phase information. In comparison, for choriocapillaris visualization, the complex OCTA is not only able to display the intensity contrast from OCT signals, but also can preserve finer details of small blood vessels with phase information and stay relatively immune to tailing artifacts.

Figure 11 shows a close look of the lobular structure of choriocapillaris. Previous histology studies have shown that the capillaries are tightly organized and separated by septaes, which can be observed as the very small black holes on OCT complex angiograms. In each lobule, there is a feeding arteriole from deeper choroid that travels parallel to the choriocapillaris plane and insert perpendicular into the capillaries lobule with a round connecting opening. In Figure 11, the connecting openings have been pointed out by red arrows. Capillaries connected to the opening are orientated in a radial fashion as histology results showed. To the best of our knowledge, this is the first time this feature has been observed by OCT complex angiograms. Figure 12 shows the OCTA images at different depth. The round opening on choriocapillaris plane pointed by red arrow in (a) is clearly connected to the deeper feeding arteriole seen on (b) and (c), which corresponds to the histological description of feeding vessels. Deeper vessels appear to be dark since there are few backscattered photons as explained before. The draining venules are located at the periphery of the lobules and in the same plane as choriocapillaris in the equatorial and more peripheral choroid. Therefore, the dark line regions on the structure images could be the draining veins as they appear to be orientated around the lobules. They are reported to be broader by Torczynski & Tso *et.al* thus further vessel diameter quantification could be useful in identifying and confirming venules in OCT complex angiograms.

Figure 13 shows the log display of choriocapillaris of the same subject. The contrast between septaes and vessels are more evident in log display but it loses dynamic range. Moreover, when comparing the macular region, linear display shows more details and therefore is selected as default display method.

Figure 14 shows the OCT complex angiogram of the other subject centered at optic nerve head. Similar lobular patterns are also observed in this subject. Different from the other subject, this scan is centered at optic nerve head therefore give more information on the equatorial region of choriocapillaris. Deeper choroidal vessels of Sattler's layer and Haller's layer have been presented in Figure 15 and Figure 16. The deeper vessels in choroid appear dark because of the weak back scattered signals. As the g factor of blood is around 0.998, the majority of the photons scatter forward in blood vessels and only a few would scatter backwards. Among those backscattered photons, only few manage to come through RPE then to interfere with lights from reference arm. Therefore, in deep choroidal tissues, the blood vessels are presented in OCTA images as dark instead of white and why the sclera appear to be white. To validate our hypothesis, we took a cube scan and investigated in the choroidal *en face* image at different depth. As showed in Figure 17, choroidal vascular network is examined at different layers. As we discussed in previous chapters, we believe that the dark patterns of choroidal vessels are due to the low signal strength from backscattered photons as the majority of the photons scattered forwardly into sclera layer. Those forward scattering photons will still carry information from choroidal vessels and will appear as tailing artifacts when we examine the *en face* OCTA images of sclera. In accordance with our hypothesis, our data shows that the big vessels in deeper choroidal tissue appear dark as in figure 17 (b) and (c), and the sclera OCTA image appear to be bright due to the tailing artifacts. In order to show the correspondence more clearly, three vessels have been manually outlines in red lines.

To conclude, OMAG – the complex OCTA approach is able to resolve the detailed lobular vascular network of choriocapillaris. With the ability to determine the feeding arterioles of choriocapillaris, OMAG is extremely helpful for the bettering understanding of choroidal circulation in pathological progresses in ocular diseases. It could essentially serve as a tool for early diagnosis of malfunction or atrophy of choriocapillaris, which could precedes the malfunction or atrophy of RPE. Different from fluorescein angiography or ICG angiography, OCT angiography relies on the intrinsic motion signal from erythrocytes therefore no exogenous contrast agents are required.

Conclusion

In this study, we demonstrated in vivo choriocapillaris imaging of healthy subjects using a Cirrus HD 5000 spectral domain OCT prototype (Carl Zeiss Meditec Inc., Dublin, CA, USA) with 68 kHz A-line acquisition speed 842 nm central wavelength. 9 mm * 11 mm OCT angiograms were generated from one tracked montage scan. Complex OMAG was used to visualize architectural morphology of choriocapillaris and our results strongly agree with previous histology studies and electron micrograph corrosion casting findings. Lobular vascular networks are clearly seen and feeding arterioles are identified and confirmed by 3D vascular network information. With the ability to visualize fine details of choriocapillaris with commercialized system, extensive clinical imaging studies are made possible to examine the role of choriocapillaris in ocular diseases such as diabetic retinopathy, age related macular degeneration or retinitis pigmentosa. With the capacity of 3D imaging of the whole posterior segment of the eye, OCTA promises to improve advance our current understanding of pathogenesis, early diagnosis and treatment monitoring of ocular diseases and could potentially revolutionized the way clinicians manage patients.

Acknowledgments

This work was supported in part by the National Institutes of Health with a contract from

National Eye Institute (R01-EY024158) and Research to Prevent Blindness (New York, NY).

References

1. Ashton, Norman. "Observations on the choroidal circulation." *The British journal of ophthalmology* 36.9 (1952): 465.
2. Flower, Robert W., Anjrez W. Fryczkowski, and D. Scott McLeod. "Variability in choriocapillaris blood flow distribution." Investigative ophthalmology & visual science 36.7 (1995): 1247-1258.
3. Nickla, Debora L., and Josh Wallman. "The multifunctional choroid." Progress in retinal and eye research 29.2 (2010): 144-168.
4. Torczynski, Elise, and Mark OM Tso. "The architecture of the choriocapillaris at the posterior pole." American journal of ophthalmology 81.4 (1976): 428-440.
5. Hayreh, Sohan Singh. "The choriocapillaris." Albrecht von Graefes Archiv für klinische und experimentelle Ophthalmologie 192.3 (1974): 165-179.
6. Weiter, John J., and J. Terry Ernest. "Anatomy of the choroidal vasculature."American journal of ophthalmology 78.4 (1974): 583-590.
7. Hayreh, SOHAN SINGH. "Segmental nature of the choroidal vasculature."British Journal of Ophthalmology 59.11 (1975): 631-648.
8. Krey, Hauke F. "Segmental vascular patterns of the choriocapillaris." American journal of ophthalmology 80.2 (1975): 198-202.
9. Wybar, Kenneth C. "A study of the choroidal circulation of the eye in man." Journal of anatomy 88.Pt 1 (1954): 94.
10. Olver, J. M. "Functional anatomy of the choroidal circulation: methyl methacrylate casting of human choroid." Eye 4.2 (1990): 262-272.
11. Sarks, J. P., S. H. Sarks, and M. C. Killingsworth. "Evolution of geographic atrophy of the retinal pigment epithelium." Eye 2.Pt 5 (1988): 552-577.
12. McLeod, D. Scott, et al. "Relationship between RPE and choriocapillaris in age-related macular degeneration." Investigative ophthalmology & visual science 50.10 (2009): 4982-4991.
13. Mullins, Robert F., et al. "Choriocapillaris vascular dropout related to density of drusen in human eyes with early age-related macular degeneration." Investigative ophthalmology & visual science 52.3 (2011): 1606.
14. Lutty, Gerard, et al. "Changes in choriocapillaris and retinal pigment epithelium in age-related macular degeneration." Mol Vis 5.35 (1999): 35.
15. FRIEDMAN, EPHRAIM, TAYLOR R. SMITH, and TOICHIRO KUWABARA. "Senile choroidal vascular patterns and drusen." Archives of Ophthalmology 69.2 (1963): 220-230.
16. Bhutto, Imran, and Gerard Lutty. "Understanding age-related macular degeneration (AMD): relationships between the photoreceptor/retinal pigment epithelium/Bruch's membrane/choriocapillaris complex." Molecular aspects of medicine 33.4 (2012): 295-317.
17. McLeod, D. Scott, et al. "Relationship between RPE and choriocapillaris in age-related macular degeneration." Investigative ophthalmology & visual science 50.10 (2009): 4982-4991.
18. Henkind, P., and S. Gartner. "The relationship between retinal pigment epithelium and the choriocapillaris." Transactions of the ophthalmological societies of the United Kingdom 103 (1982): 444-447.
19. Gerl, Verena B., et al. "Extensive deposits of complement C3d and C5b-9 in the choriocapillaris of eyes of patients with diabetic retinopathy." Investigative ophthalmology & visual science 43.4 (2002): 1104-1108.
20. Cao, Jingtai, et al. "Choriocapillaris degeneration and related pathologic changes in human diabetic eyes." Archives of ophthalmology 116.5 (1998): 589-597.
21. Hyvarinen, Lea, et al. "Fluorescein angiography of the choriocapillaris." American journal of

ophthalmology 67.5 (1969): 653-666.
22. Hayashi, Kazuhiko, Yutaka Hasegawa, and Takashi Tokoro. "Indocyanine green angiography of central serous chorioretinopathy." International ophthalmology 9.1 (1986): 37-41.
23. Pauleikhoff, Daniel, et al. "A fluorescein and indocyanine green angiographic study of choriocapillaris in age-related macular disease." Archives of ophthalmology 117.10 (1999): 1353-1358.
24. Huang, David, et al. "Optical coherence tomography." Science 254.5035 (1991): 1178-1181.
25. Tomlins, Peter H., and R. K. Wang. "Theory, developments and applications of optical coherence tomography." Journal of Physics D: Applied Physics 38.15 (2005): 2519.
26. Marschall, Sebastian, et al. "Optical coherence tomography—current technology and applications in clinical and biomedical research." Analytical and bioanalytical chemistry 400.9 (2011): 2699-2720.
27. Wang, Ruikang K., et al. "Three dimensional optical angiography." Optics express 15.7 (2007): 4083-4097.
28. Baran, Utku, et al. "High resolution imaging of acne lesion development and scarring in human facial skin using OCT-based microangiography." Lasers in surgery and medicine 47.3 (2015): 231-238.
29. Zagaynova, E., et al. "Endoscopic OCT with forward-looking probe: clinical studies in urology and gastroenterology." Journal of biophotonics 1.2 (2008): 114-128.
30. Arevalo, J. Fernando, ed. Retinal angiography and optical coherence tomography. Springer New York, 2009.
31. Ikuno, Yasushi, et al. "Choroidal thickness in healthy Japanese subjects." Investigative ophthalmology & visual science 51.4 (2010): 2173-2176.
32. Tan, Colin S., et al. "Diurnal variation of choroidal thickness in normal, healthy subjects measured by spectral domain optical coherence tomography." Investigative ophthalmology & visual science 53.1 (2012): 261-266.
33. Maruko, Ichiro, et al. "Subfoveal choroidal thickness after treatment of central serous chorioretinopathy." Ophthalmology 117.9 (2010): 1792-1799.
34. Manjunath, Varsha, et al. "Choroidal thickness in normal eyes measured using Cirrus HD optical coherence tomography." American journal of ophthalmology 150.3 (2010): 325-329.
35. Koizumi, Hideki, et al. "Subfoveal choroidal thickness in typical age-related macular degeneration and polypoidal choroidal vasculopathy." Graefe's Archive for Clinical and Experimental Ophthalmology 249.8 (2011): 1123-1128.
36. Giovannini, A., et al. "OCT imaging of choroidal neovascularisation and its role in the determination of patients' eligibility for surgery." British journal of ophthalmology 83.4 (1999): 438-442.
37. KERCKHOVEN, VAN. "Features of age-related macular degeneration on optical coherence tomography." Bull. Soc. belge Ophtalmol 281 (2001): 75-84.
38. Hee, Michael R., et al. "Optical coherence tomography of age-related macular degeneration and choroidal neovascularization." Ophthalmology 103.8 (1996): 1260-1270.
39. Kurokawa, Kazuhiro, et al. "Three-dimensional retinal and choroidal capillary imaging by power Doppler optical coherence angiography with adaptive optics." Optics express 20.20 (2012): 22796-22812.
40. Braaf, Boy, et al. "Phase-stabilized optical frequency domain imaging at 1-µm for the measurement of blood flow in the human choroid." Optics express 19.21 (2011): 20886-20903.
41. Choi, WooJhon, et al. "Choriocapillaris and choroidal microvasculature imaging with ultrahigh speed OCT angiography." (2013): e81499.

Figures

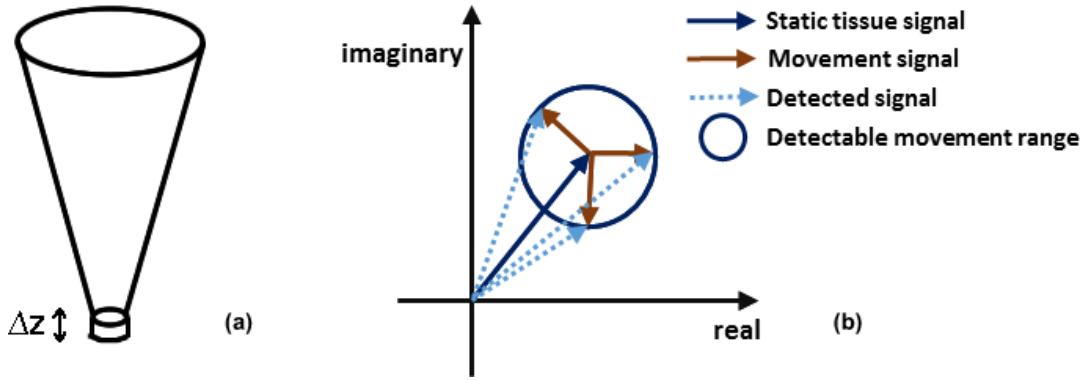

Figure 1. Illustration of OCT signal. (a) shows the focal spot of OCT on tissue; (b) shows the OCT signal in complex coordinates.

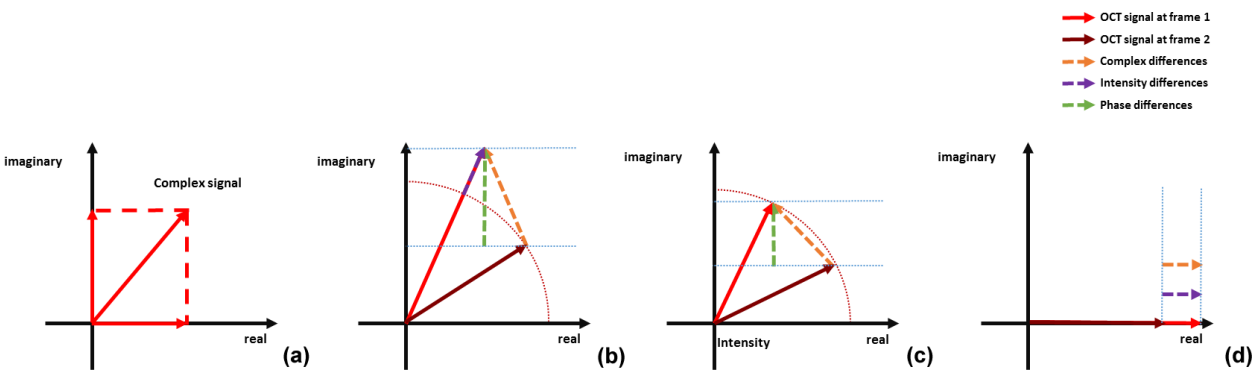

Figure 2. Illustration of OCT signal at a time interval on the same location. (a) OCT signal in complex coordinates; (b) – (d) three different case scenarios to compare the signal strength on intensity approach, phase approach and complex approach.

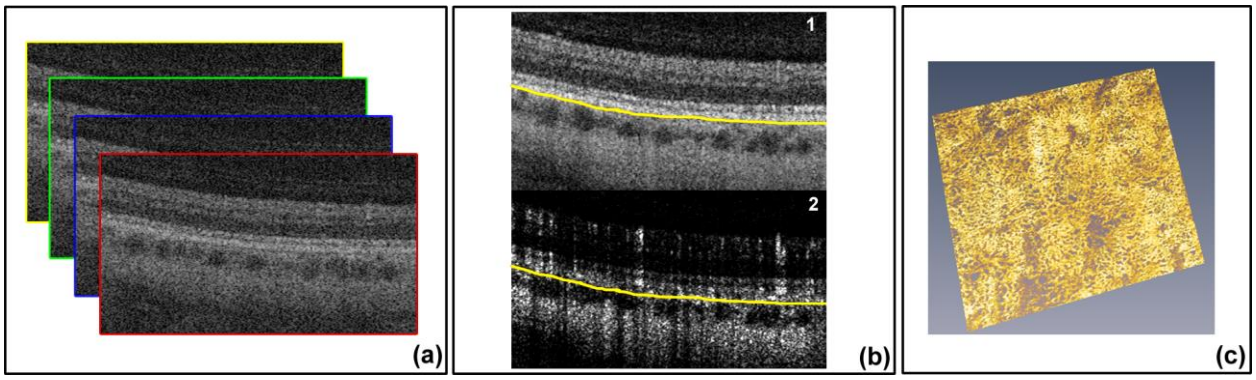

Figure 3. Illustration of OMAG algorithms and 3D visualization of choriocapillaris.

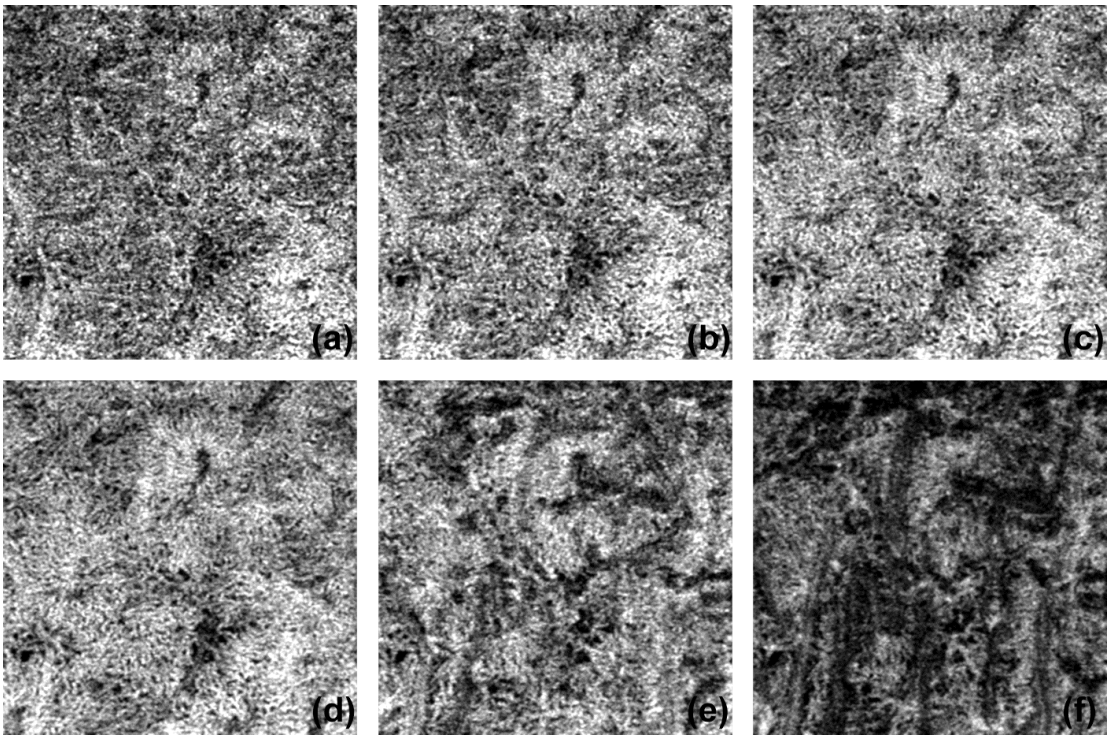

Figure 4. Choriocapillaris slab foe different thickness along z depth. (a) shows a 2.2 μm slab under Bruch's membrane; (b) shows a 6.6 μm slab under Bruch's membrane; (c) shows a 11 μm slab under Bruch's membrane; (d) shows a 17.6 μm slab under Bruch's membrane; (e) shows a 11 μm thick slab at 20 μm under Bruch's membrane; (f) shows a 11 μm thick slab at 30 μm under Bruch's membrane;

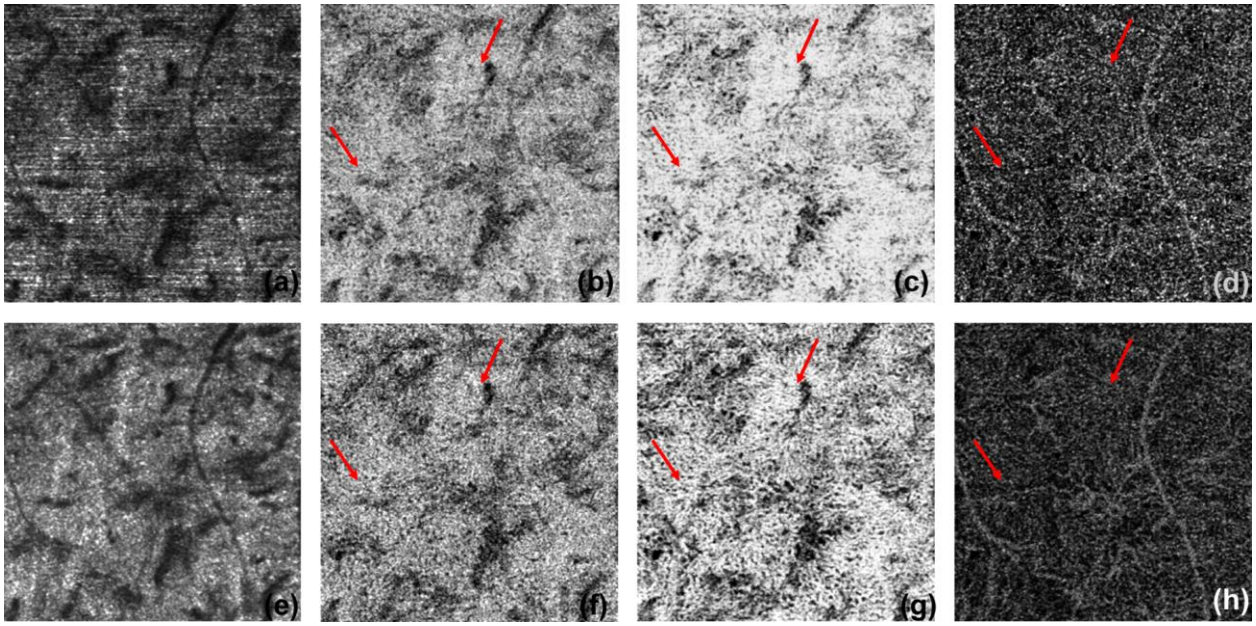

Figure 5. Comparison between arithmetic mean approach and arithmetic mean, geometric mean combined approach. (a) – (d) are structure, intensity flow, complex flow and phase flow en face images with only AM approach. (e) – (h) are structure, intensity flow, complex flow and phase flow en face images with AM, GM combined approach.

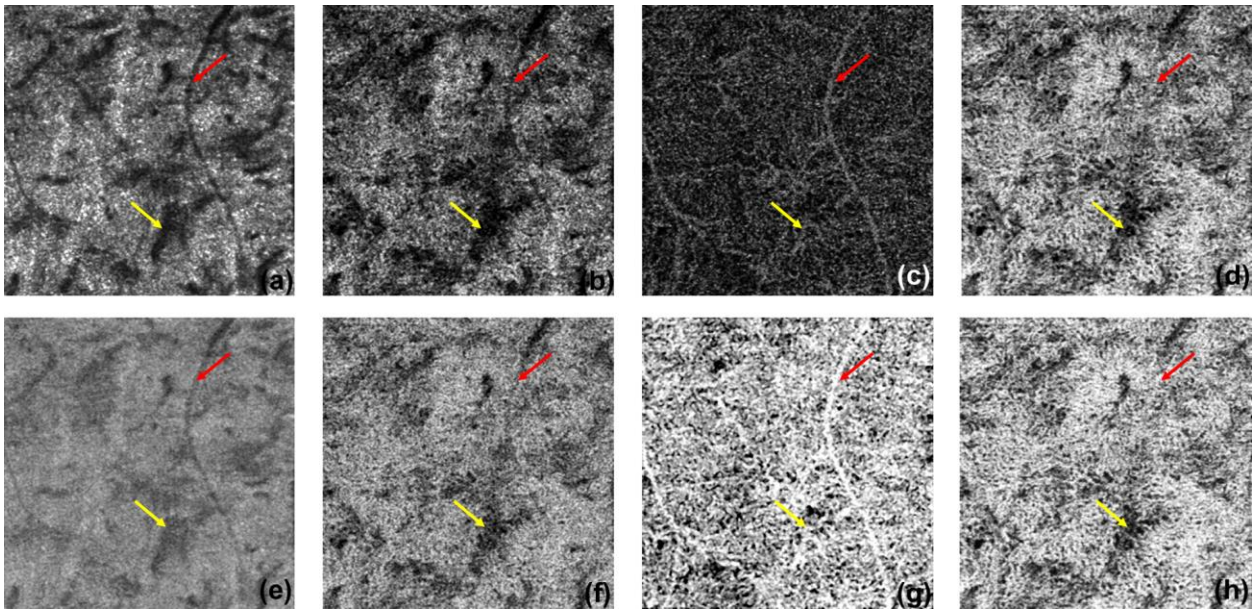

Figure 6. Comparison of choriocapillaris visualization with intensity, phase and complex approaches. (a) – (d) are linear display of OCT structure, intensity OCTA, phase OCTA and complex OCTA respectively; (e) – (h) are log display of OCT structure, intensity OCTA, phase OCTA and complex OCTA respectively.

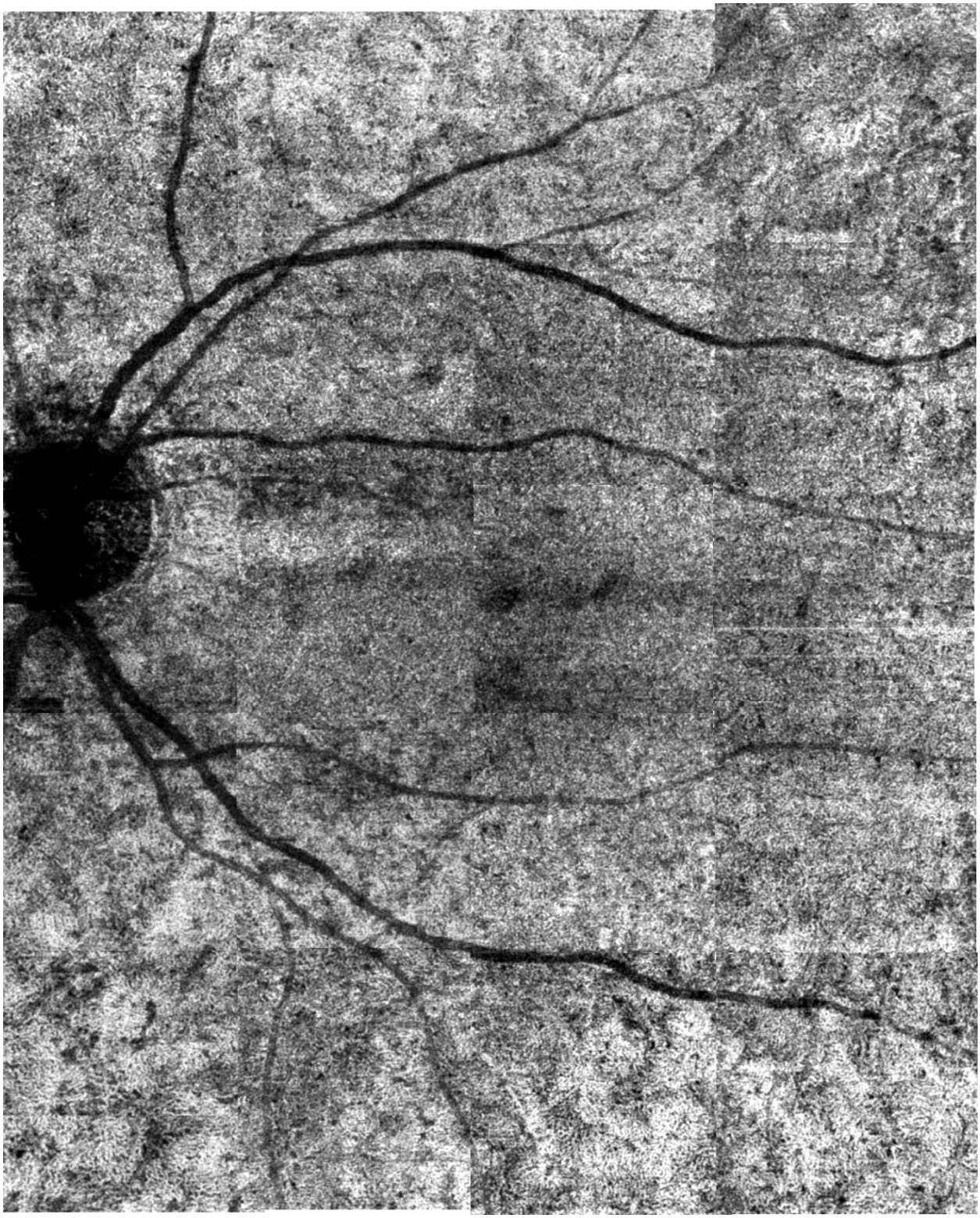

Figure 7

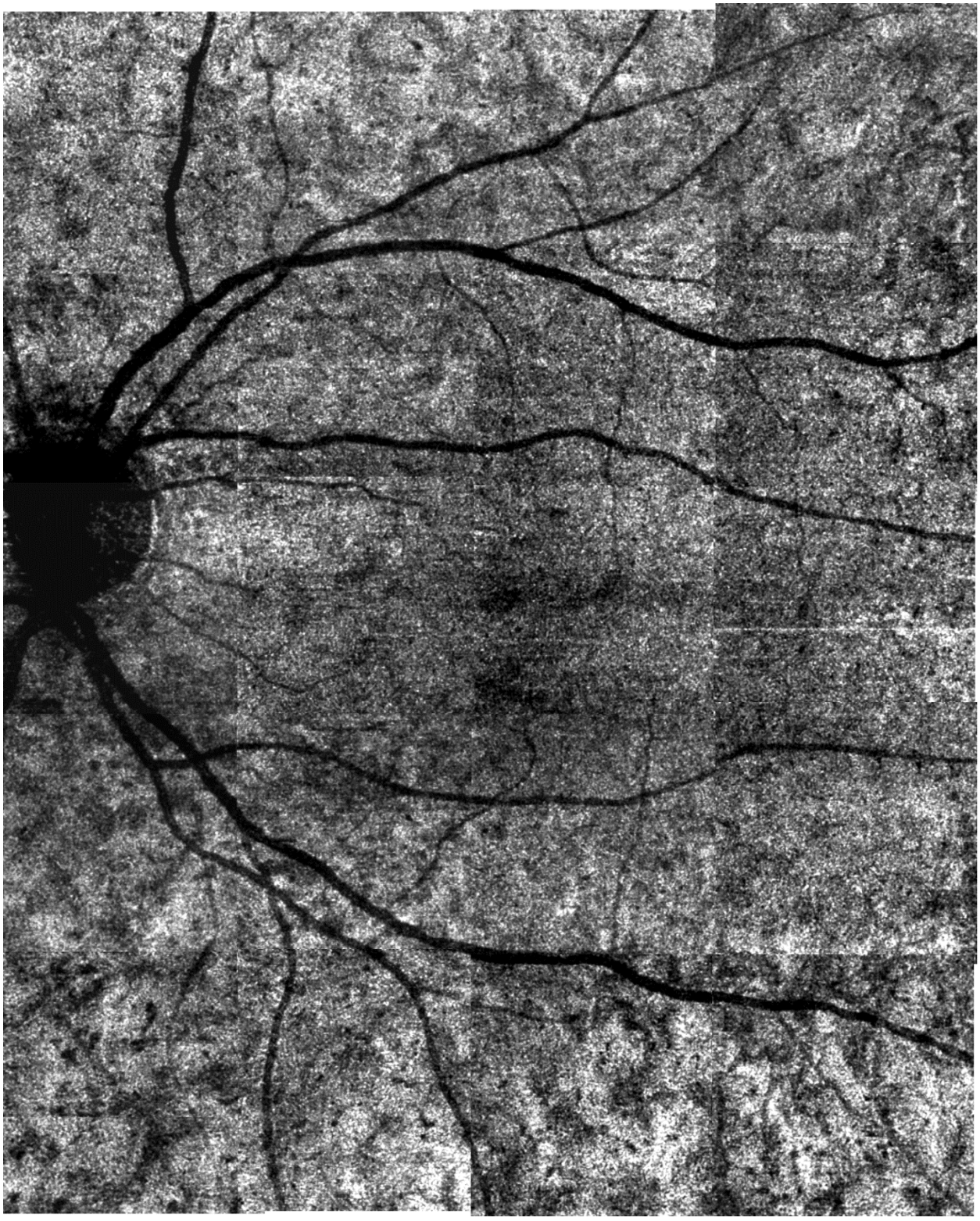

Figure 8

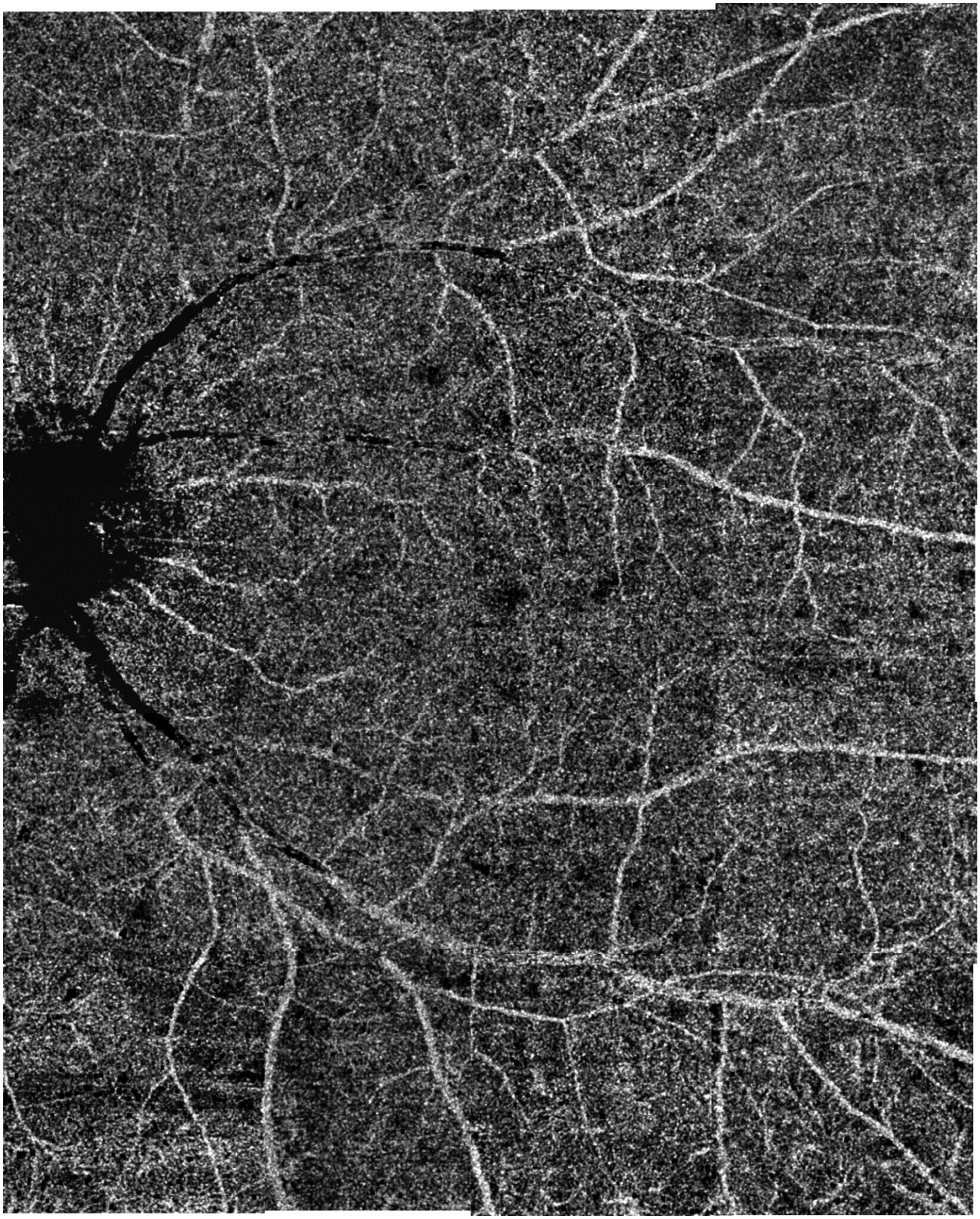

Figure 9

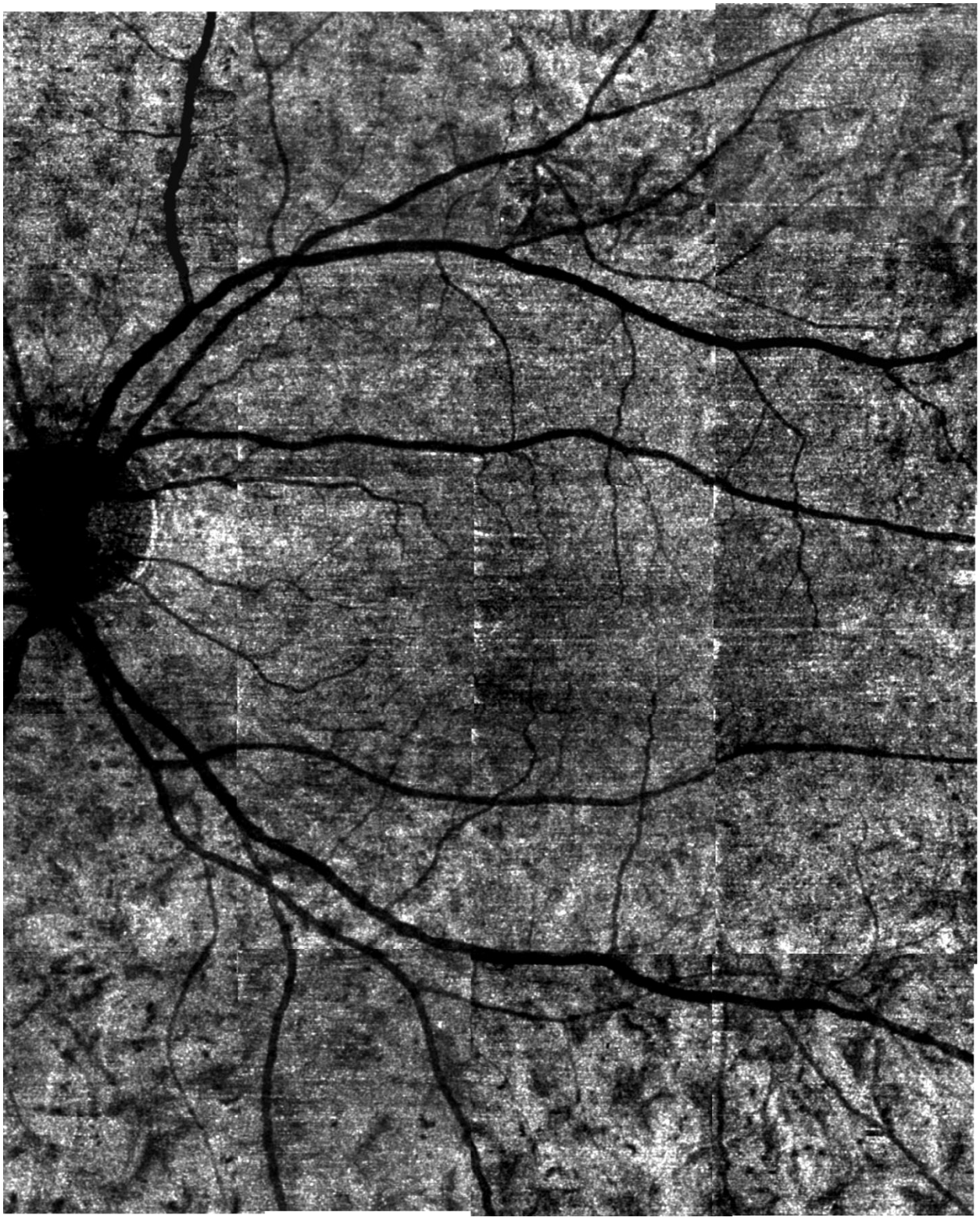

Figure 10

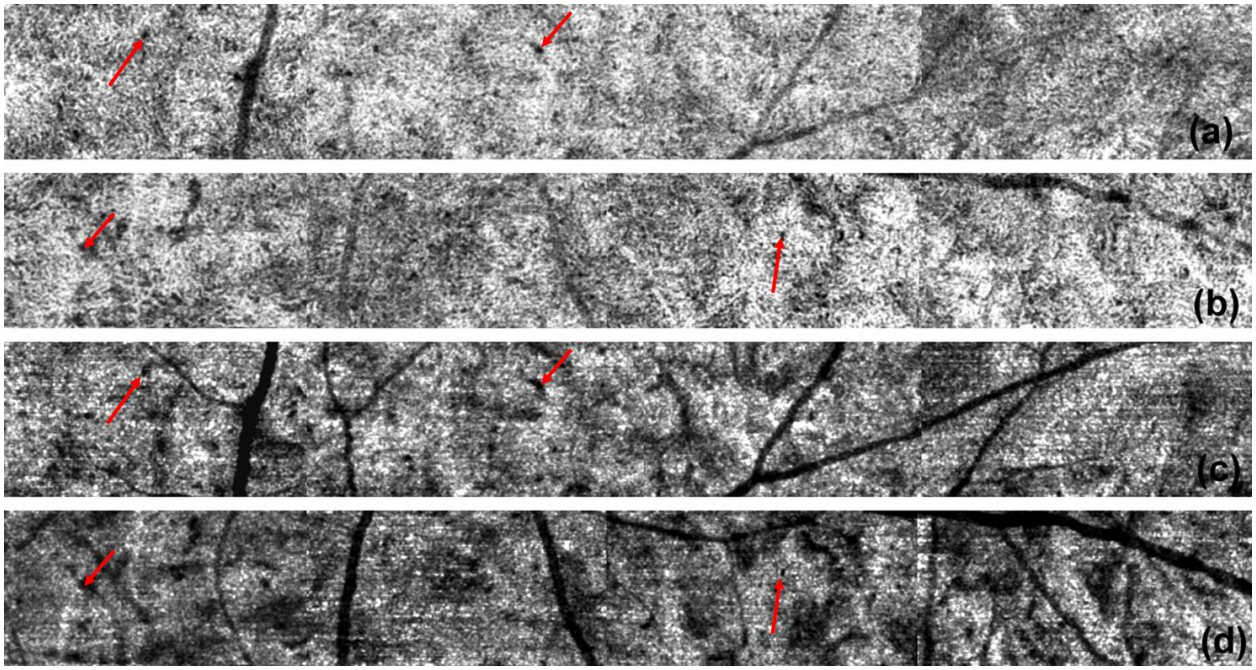

Figure 11. OCT complex angiogram of periphery regions.(a) is the OCT complex angiogram of superior region; (b) is the OCT complex angiogram of inferior region; (c) and (d) are the OCT structural *en face* images of (a) and (b) respectively. Red arrows point to connection of choriocapillaris and feeding arterioles.

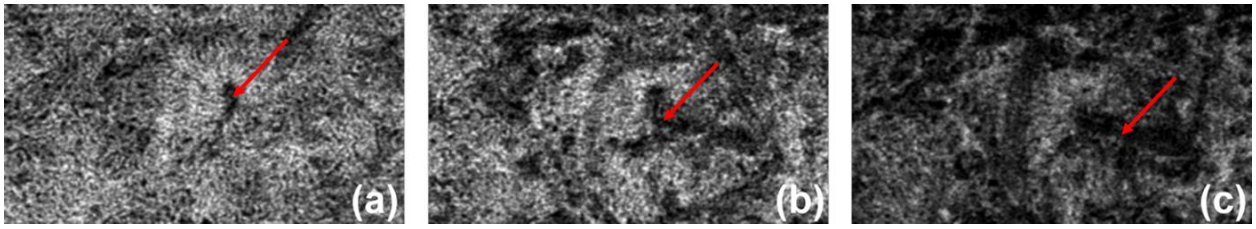

Figure 12. OCT complex angiogram at different depth. (a) shows a 17.6 μm choriocapillaris slab under Bruch's membrane; (b) shows a 11 μm thick slab under the choriocapillaris slab; (c) shows a 11 μm thick slab under (b).

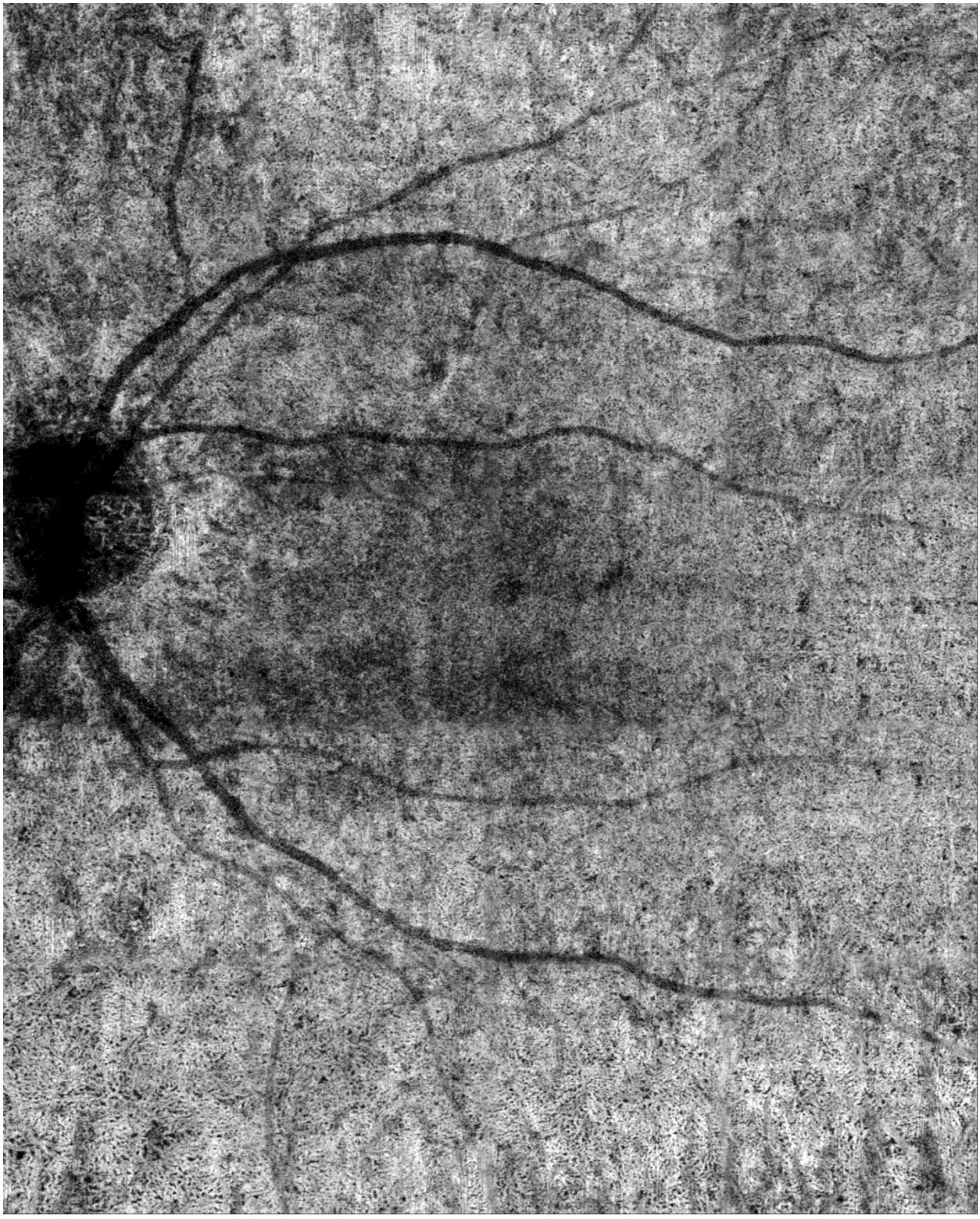

Figure 13

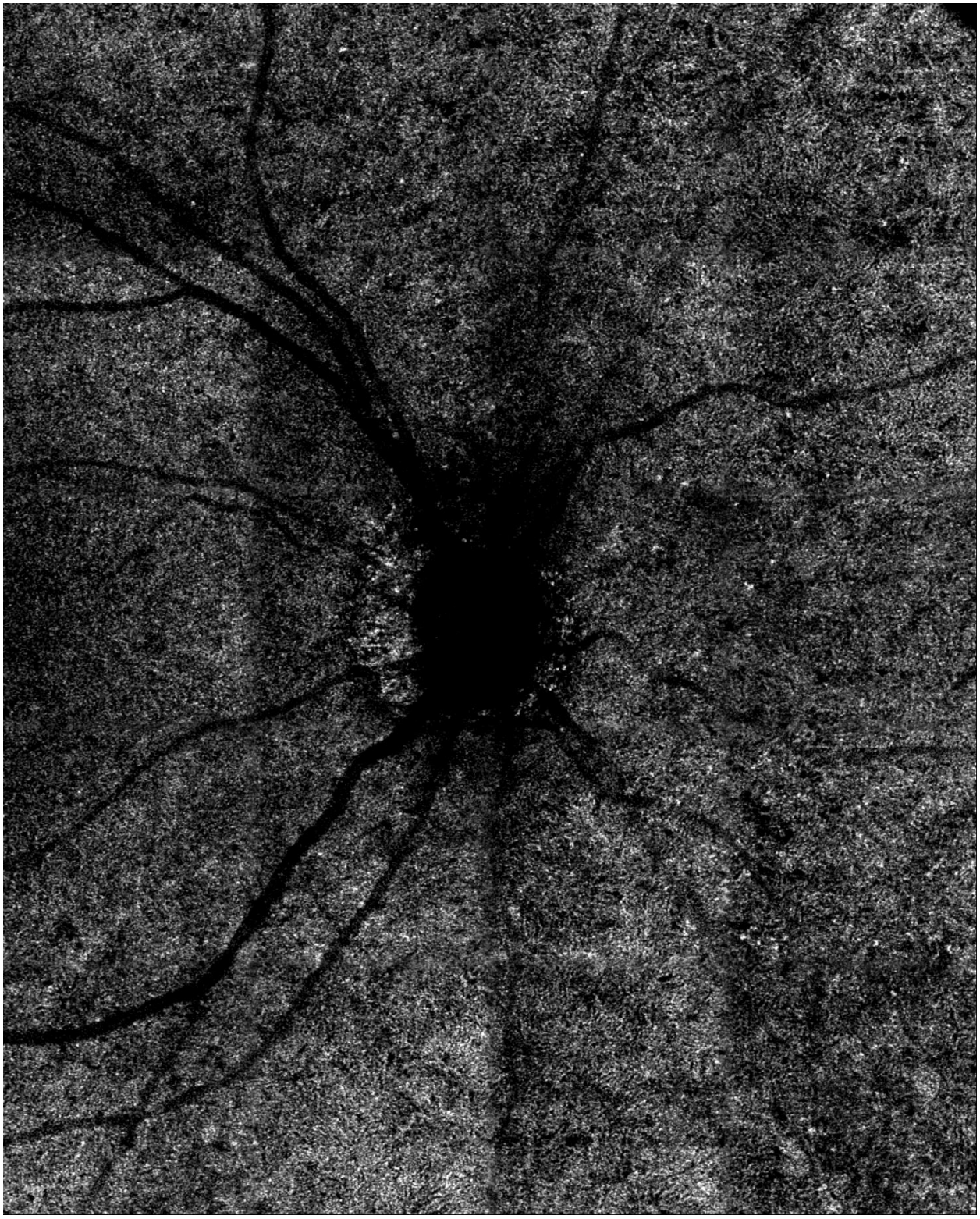

Figure 14 Choriocapillaris *en face* visualization of the other subject, centered at optic nerve head.

Repeatability and Reproducibility of 3D Choroidal Topographic Maps for thickness measurement with 1050nm Ultrawide-field Enhanced Depth Imaging SD-OCT

Abstract

Purpose: The aim of this study is to demonstrate a new three-step strategy of choroidal thickness measurement with higher repeatability and reproducibility. An accurate choroidal topographic map was generated and utilized in thickness measurement by using 1050-nm 147 kHz ultrawide-field SD-OCT with imaging depth of 6.1mm.

Methods: Nine volunteers' nine eyes have been scanned repeatedly three times each eye and one volunteer's one eye has been scanned three times per day for three days, in total 36 data sets have been acquired, covering an $8 \times 8 \times 6$ cm^3 3D volume each. A three-step strategy has been employed to generate one choroidal topographic map for each eye using information from six sets of maps from three scans for choroidal thickness measurement.

Results: 3D data volume have been flattened for both direction on transverse plane before choroidal topographic maps were generated from both B-scan direction and C-scan direction and averaged, then three maps from three scan of one eye were spatially averaged to further reduce errors. Statistical analysis has been conducted to validate that our proposed choroidal thickness measurement method generates results with a significantly lower standard deviation and C.V between scans of the same eye.

Conclusions: We have proposed and validated our three-step strategy of measuring choroidal thickness using choroidal topographic map, this method is especially suitable for monitoring

chorioretinal diseases development with short time intervals as the choroid abnormality would be accurately recorded with our method.

Introduction

Choroid is a highly vascularized layer with connective tissue, pigment and intrinsic neurons that lies between retina and sclera. As the tissue with the highest blood flow per unit in human body[1], choroid provides oxygen and nutrients to the outer retina as well as retinal pigment epithelium (RPE). With the proximity of retina, choroid plays a crucial role in many ocular disease processing such as age-related macular degeneration (AMD), glaucoma and diabetic retinopathy. Choroidal neovascularization (CNV) happens in various ocular diseases as well as in pathological myopia, usually resulted in choroidal thickness change[2,3]. Studies[4] show that subfoveal choroidal thickness (SFCT) increase as the severity worsened from nonproliferative diabetic retinopathy (NPDR) to proliferative diabetic retinopathy (PDR). It's been reported[5,6] that highly myopic eyes' choroidal thickness and retinal thickness are statistically significantly thinner than non-myopic age matched eyes and choroidal thickness is related to vision acuity.

Spectral domain Optical Coherence Tomography (SD-OCT) is a noninvasive real-time cross-sectional imaging technique for volumetric imaging of internal structures of biological systems in vivo with ultra-high resolution, sensitivity and imaging speed. Due to the easy optical access to the posterior segments of the eye, OCT has become a widely used imaging technique in ophthalmic imaging for various purpose[7-9]. As choroid is composed 95% of blood vessels, choroidal thickness has been reported can change promptly on ocular abnormality and myopia[10]. However, due to the highly scattering property of RPE layer in retina and SD-OCT system sensitivity roll-off at deep choroid layer, choroidal imaging and CT measurement are tricky and

erroneous. Along the innovate development of OCT ophthalmic imaging, enhance depth imaging (EDI) technique[11] has been introduced to compensate for the depth related sensitivity roll-off in choroidal imaging. Still, studies show that the accuracy of CT measurement are vulnerable to intraobserver and interobserver measurement as well as use of 1:1 pixel image or 1:1 micron image, due to the limit of OCT system imaging depth, scanning density, image pixel size and lacking of reliable automated segmentation method[12,13].

In this paper, we report a new method of choroidal thickness measurement using choroidal topographic maps with a significant improvement on the repeatability and consistency of choroidal thickness measurement that is especially suitable for within case monitoring using a home built 1050nm ultra-wide field spectral domain optical coherence tomography at 147 kHz A-scan rate with 6.1mm imaging depth.

Methods

We used a newly developed 1050nm SD-OCT as has been described in detail before [14], the system configuration is illustrated in Fig.1. A 1050nm ASE module (Amonics, ALS-1050-20) light source with ~20mW (~1.8mW in sampler arm after a 10/90 fiber coupler) output power has been employed to deliver an axial resolution of ~10μm in the air (7.4μm in tissue) and an lateral resolution of ~15μm in the air (11.1μm in tissue) with a 50nm bandwidth while a linescan InGaAs camera (Sensors Unlimited Inc. (SUI), a United Technologies Aerospace Systems company, New Jersey, USA) with 2048 photodiode array capable of 147 kHz line-scan rate is employed within the home built spectrometer to achieve the high speed imaging speed. With the x-y 2D galvanometer scanning system, a large field of view of 8×8mm and imaging depth of 6.1mm.

With the SD-OCT system previously described, we performed in vivo real-time 3D posterior segment eye imaging with 5 eyes. The x-y galvanometer scanning system and high speed camera enables the acquisition of large-field-of-view 3D data in 2 seconds with 512 A-lines in the fast scan direction and 512 B frames in the slow scan direction, with 1024 pixel each A-line, covering a $8 \times 8 \times 6$ cm^3 space in human eye posterior segment. Fig.2 (a) is a typical SD-OCT *en face* image while Fig.2 (b) is an averaged cross sectional B-scan frame for thin choroid, the choroid sclera junction is resolved clearly, Fig.2 (c) is an averaged B-scan frame for thick choroid, which could be hard to visualize due to the inevitable light attenuation and scattering, enhanced depth imaging technique has been employed to better resolve the choroid&scelar junction. The definition of choroidal thickness is the vertical distance from the posterior edge of the RPE layer to the inner sclera border, whose measurement could be intrinsically erroneous due the light scattering and attenuation induced image quality degradation, limited axial resolution and pixel size axially induced fluctuation between scans and subjective differences introduced between observers. These systemic and operational error could lead to false positive or false negative results on choroidal thickness changes in clinical study especially for within case monitoring as the changes over short time interval could be buried within errors. Thus we propose to perform a three-step strategy to measurement choroidal thickness with higher accuracy and repeatability.

Three healthy volunteers have been scanned by our SD-OCT, using enhanced depth imaging technique, putting the zero-delay line behind the RPE layer by moving the reference mirror, 3D data sets of 5 eyes of $512 \times 512 \times 1024$, covering a volume of $8mm \times 8mm \times 6mm$, repeating three times for each eye that haven been acquired. Segmentation has been performed by one well-trained OCT reader and used for choroidal topography map generation and choroidal thickness measurement. The segmentation of the 3D data set was performed twice as the first time on

unpreprocessed data and the second time on preprocessed data, masked to previous segmentation result.

Results

Fig.3(a) is a typical 3D volumetric rendering image of captured data while 3(b) is a typical B-scan frame and 3(c) is a typical C-scan frame. Due to the inevitable subject movement, motion artifacts can be easily observed in C-scans as fig. 3(c), and the retina curvature can be easily observed in B-frames as fig. 3(b). Which both could complicate the process of choroidal thickness measurement, especially for intervisit scans of same subject. In order to compensate for the retina curvature as well as the inevitable subject movement, two processes have been employed. We firstly performed motion artifacts correction within B-frames by employing a cross-correlation algorithm by calculating the cross-correlation map to determine the displacement of adjacent three B-frames then compensate for each B-frame by correcting the displacement then averaging. After this step, we performed another strategy to furthermore compensate the retina curvature. We firstly created a 3D map of retina curvature as showed in fig. 3(e), in doing so, the RPE layer was extracted as showed by the red line in (b) and its pixel position has been recorded, which provides information of the axial displacement of each A-line due to the retina curvature, as showed in fig. 3 (e), a 512×512 map with false color representing the curvature displacement. Then each A-line in this 3D volume has been given the axial displacement distance to compensate for the curvature. After this process, each B-frame as showed in fig.3 (f), has been successfully compensated for the retina curvature as well as each C-scans as showed in fig. 3(g). Thus the whole 3D volume has been flattened as showed in Fig.3 (d).

As the red lines showed in Fig. 4(a), the RPE layer and the inner sclera border at the choroid&sclear junction was determined manually by well-trained OCT reader and used for choroidal topography map generation and choroidal thickness measurement. After 3D volume segmentation, choroidal topographic maps were generated to visualize choroidal thickness as showed in Fig.4(c) to present the choroidal thickness in a more comprehensive way. As the imaging depth 6.1mm is represented by 1024 pixel, the pixel size axially is calculated to be 4.41 (assuming the refractive index to be 1.35). To further improve the accuracy of choroidal thickness measurement, another measurement have been conducted by the same engineer by the same protocol but in the transverse direction by going through each C-scan (Fig. 3(g)). The choroidal topographic map along C-scan direction is showed in Fig.4 (d). As can be clearly observed in Fig. 4(c)and (d), the B-scan based map tend to have a clearer horizontal line pattern while the latter C-scan based map tend to show a vertical line pattern. To further reduce human factor errors, the final choroidal topographic map was an averaged result of the B-scan based map and C-scan based map as showed in Fig. 4(e) with the color bar marked in μm. Three concentric rings have been generated on the map with diameters of 1mm, 3mm and 6mm respectively to label out the central fovea region (1mm), parafovea region (3mm, inner ring) and perifovea region (6mm, outer ring) and 4 quadrants have also been labeled (superior, inferior, temporal and nasal). The retinal topographic map generated by the same protocol as the choroidal topographic map was used to determine the position of the center of the fovea, which has the lowest thickness as showed in Fig. 4(b). Thus our region of interest has been divided into 9 subfields (parafovea temporal, perifovea temporal, central fovea, perifovea nasal and parafovea nasal from left to right and parafovea superior, perifovea superior, central fovea, perifovea inferior and parafovea inferior from top to bottom) to better characterize the choroidal topographic as showed in Fig. 4(e) as well as confirmed by retinal topographic map Fig.4 (b). Thus we have described in detail the process of generating choroidal topographic map for one 3D scan.

In total 15 3D data sets were acquired from three volunteer subjects as 3 scans each eye for 5 eyes, choroidal topographic maps were generated for choroidal thickness measurement with our proposed preprocessing method as well as by directly measuring from 3D data sets along naturally direction, B-scan direction without preprocessing. In with preprocessing method, three choroidal topographic maps were generated for each scan as a result of averaging B-scan based map and C-scan based map while so are three maps generated for measurement without preprocessing. In order to evaluate the accuracy and repeatability of our proposed method and normal method, intermethod comparisons for both nasal-temporal measurement and superior-inferior measurement were conducted, result of mean of choroidal thickness and standard deviation of measurements are showed in Fig.6.

Fig.6(a) shows the mean and standard deviation of choroidal thickness measurement for 5 eyes without preprocessing, it can be clearly observed that for eye 1-3, the standard deviation is quite high compared to the measurement of eye 1-3, with preprocessing method in Fig. 6(b). Similar conclusion can also be drawn from the comparison in superior-inferior direction. It can also be observed that choroidal thickness measurements tend to be more erroneous for thicker choroid as have been previously reported [15]. The standard deviation of each measurements (3 scans for one eye) have also been calculated as showed in Table 1. One way ANOVA analysis of mean values of choroidal thickness measurements of two methods have been conducted as the result indicates that our proposed method of measuring choroidal thickness have a significantly lower standard deviation between scans of the same eye, also the summary of coefficient of variance have been provided in Table 2, the C.V of our proposed method is obviously much lower than before, thus provides a higher repeatability of choroidal thickness measurement.

As we have mentioned in the scanning protocol, each eye was scanned repeatedly three times with a time interval of 30 seconds for the subjects to relax and rest, thus three choroidal topographic maps were generated for each eye as showed in Fig. 5. (a)-(c), similar patterns can be observed clearly between these choroidal topographic maps and it's quite clear that systemic and operational errors can be reduced further by averaging these three maps. Due to the inevitable eye ball movement during the 30 seconds time interval, we performed spatially averaging with motion correction for those three consecutive scans of one eye. In order to do so, we used three retinal topographic maps of the same scan data set to determine the displacement distance along both directions in transvers plane for these three data sets by using cross-correlation algorithm for the reason that retina structure features are simpler and easier to identify than choroid, then the same displacement correction haven been applied to choroidal topographic maps, then three choroidal topographic maps were averaged as showed in Fig. 5(d), choroidal thickness was calculated by averaging the thickness value of the whole area for each subfield and presented in each subfield.

Conclusion

In this study, we proposed a new method of choroidal thickness measurement by using choroidal topographic maps. We demonstrated a three-step preprocessing method of generating choroidal topographic maps consisting of 3D data set flattening on both B-scan direction and C-scan direction; choroidal topographic map of one scan generated by averaging two direction segmentation (B-scan based segmentation and C-scan based segmentation) and spatially averaging three scans generated choroidal topographic maps for final choroidal topographic map for one eye. Choroidal thickness of 5 eyes from three healthy volunteers have been measured through choroidal topographic maps generated with our proposed method and with current popular method without preprocessing and averaging, statistical analysis showed our method

enables a smaller standard deviation as well as coefficient of variance within measurements of multiple scans of one subject one time. Thus, we propose that this new method would be especially useful in monitoring various chorioretinal diseases development process of same patient as the choroid abnormalities would be picked up as true positive changes instead of false positive results due to inevitable systemic and operational errors.

References

1. Alm, Albert, and Anders Bill. "Ocular and optic nerve blood flow at normal and increased intraocular pressures in monkeys (< i> Macaca irus</i>): a study with radioactively labelled microspheres including flow determinations in brain and some other tissues." Experimental eye research 15.1 (1973): 15-29.
2. Manjunath, Varsha, et al. "Analysis of choroidal thickness in age-related macular degeneration using spectral-domain optical coherence tomography." American journal of ophthalmology 152.4 (2011): 663-668.
3. Koizumi, Hideki, et al. "Subfoveal choroidal thickness in typical age-related macular degeneration and polypoidal choroidal vasculopathy." Graefe's Archive for Clinical and Experimental Ophthalmology 249.8 (2011): 1123-1128.
4. Kim, Jee Taek, et al. "Changes in choroidal thickness in relation to the severity of retinopathy and macular edema in type 2 diabetic patients." Investigative ophthalmology & visual science 54.5 (2013): 3378-3384.
5. GROSSNIKLAUS, HANS E., and W. RICHARD GREEN. "Pathologic findings in pathologic myopia." Retina 12.2 (1992): 127-133.
6. Flores-Moreno, Ignacio, et al. "The relationship between retinal and choroidal thickness and visual acuity in highly myopic eyes." British Journal of Ophthalmology (2013).
7. An, Lin, and Ruikang K. Wang. "In vivo volumetric imaging of vascular perfusion within human retina and choroids with optical micro-angiography." Optics Express 16.15 (2008): 11438-11452.
8. Esmaeelpour, Marieh, et al. "Three-dimensional 1060-nm OCT: choroidal thickness maps in normal subjects and improved posterior segment visualization in cataract patients." Investigative ophthalmology & visual science 51.10 (2010): 5260-5266.
9. Zhang, Qinqin, et al. "Geographic Mapping of Choroidal Thickness in Myopic eyes using 1050-nm Spectral Domain Optical Coherence Tomography." Journal of Innovative Optical Health Sciences (2014).
10. Fitzgerald, Malinda EC, Christine F. Wildsoet, and Anton Reiner. "Temporal relationship of choroidal blood flow and thickness changes during recovery from form deprivation myopia in chicks." Experimental eye research 74.5 (2002): 561-570.
11. Spaide, Richard F., Hideki Koizumi, and Maria C. Pozonni. "Enhanced depth imaging spectral-domain optical coherence tomography." American journal of ophthalmology 146.4 (2008): 496-500.
12. Rahman, Waheeda, et al. "Repeatability of manual subfoveal choroidal thickness measurements in healthy subjects using the technique of enhanced depth imaging optical coherence tomography." Investigative ophthalmology & visual science 52.5 (2011): 2267-2271.
13. Fong, Angie HC, Kenneth KW Li, and David Wong. "Choroidal evaluation using enhanced depth imaging spectral-domain optical coherence tomography in Vogt–Koyanagi–Harada disease." Retina 31.3 (2011): 502-509.
14. An, Lin, et al. "High-resolution 1050 nm spectral domain retinal optical coherence tomography at 120 kHz A-scan rate with 6.1 mm imaging depth." Biomedical optics express 4.2 (2013): 245-259.

15. Cho, A. R., Y. J. Choi, and Y. T. Kim. "Influence of choroidal thickness on subfoveal choroidal thickness measurement repeatability using enhanced depth imaging optical coherence tomography." Eye (2014).

Tables

Table 1 Summary of standard deviations of each eye for all three measurements and calculated one way ANOVA p-value

	subject1 OS	subject1 OD	subject2 OS	subject2 OD	subject3 OS	
			standard deviation			*p-value*
unpreprocessed	10.1263	14.03	10.9368	6.1309	7.1414	0.0012
preprocessed	1.9388	3.3828	2.9504	1.8881	2.9241	

Table 2 Summary of coefficient of variance with two methods of each eye for all three measurements.

	subject1 OS	subject1 OD	subject2 OS	subject2 OD	subject3 OS	
			C.V			*average*
unpreprocessed	0.026	0.0335	0.0274	0.0262	0.0265	0.02792
preprocessed	0.0048	0.0082	0.0071	0.0078	0.011	0.00778

Figures

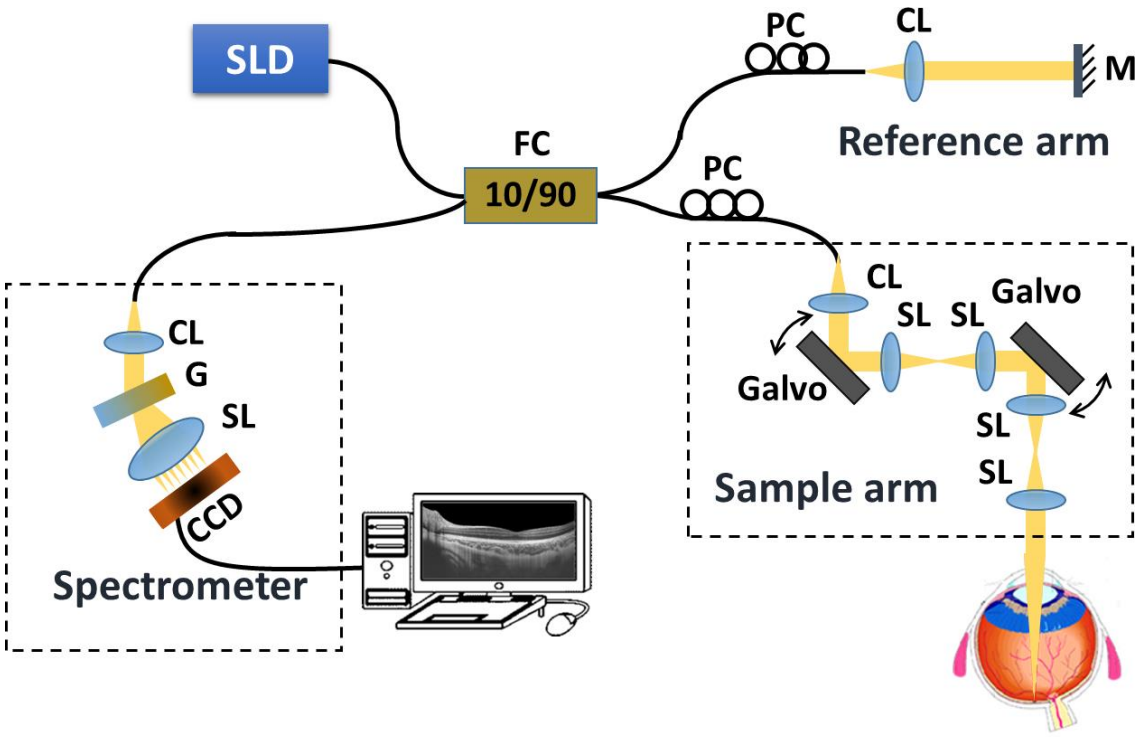

Fig. 1. Schematic of the SD-OCT system setup. SLD: 1.0 μm superluminescent diode; FC: fiber optic coupler; CL: collimating lens; SL: scan lens; G: grating; PC: polarization controller; M: reference mirror.

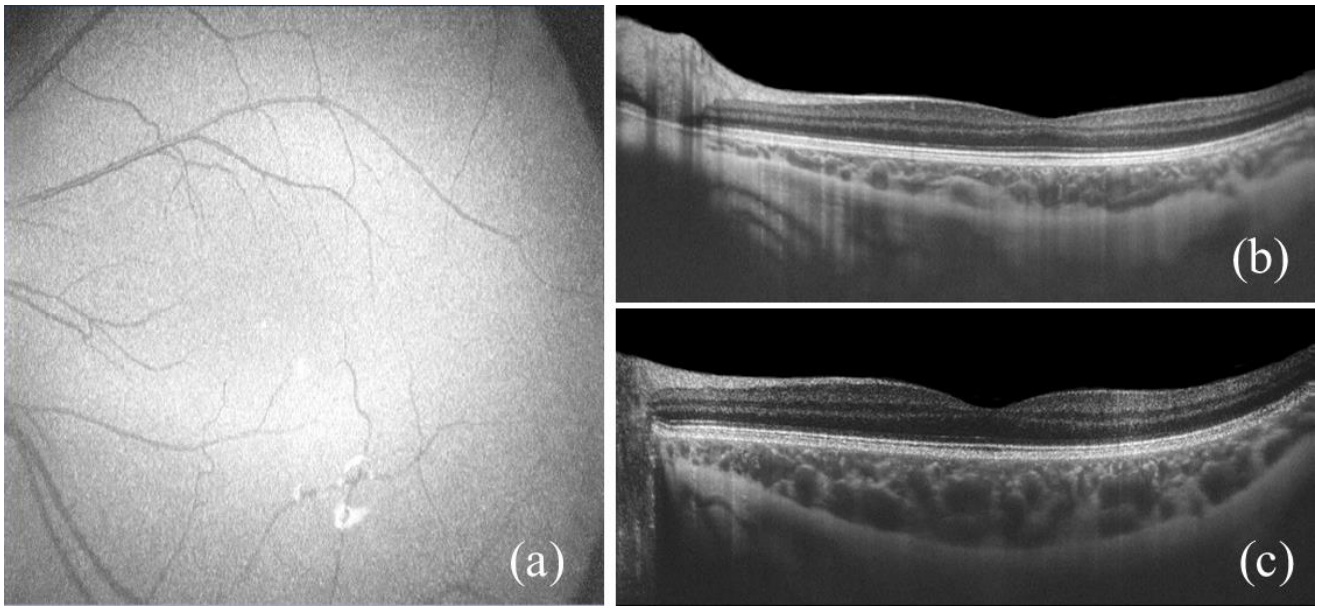

Fig. 2. Retina curvature and movement compensation for 3D volume data. (a) typical 3D volume data acquired by the SD-OCT; (b) typical B-scan with red line marked as RPE layer; (c) typical C-scan without preprocessing; (d) typical 3D volume data after compensation; (e) typical retina curvature map; (f) typical B-scan after curvature compensation; (g) typical C-scan after both movement compensation and curvature compensation.

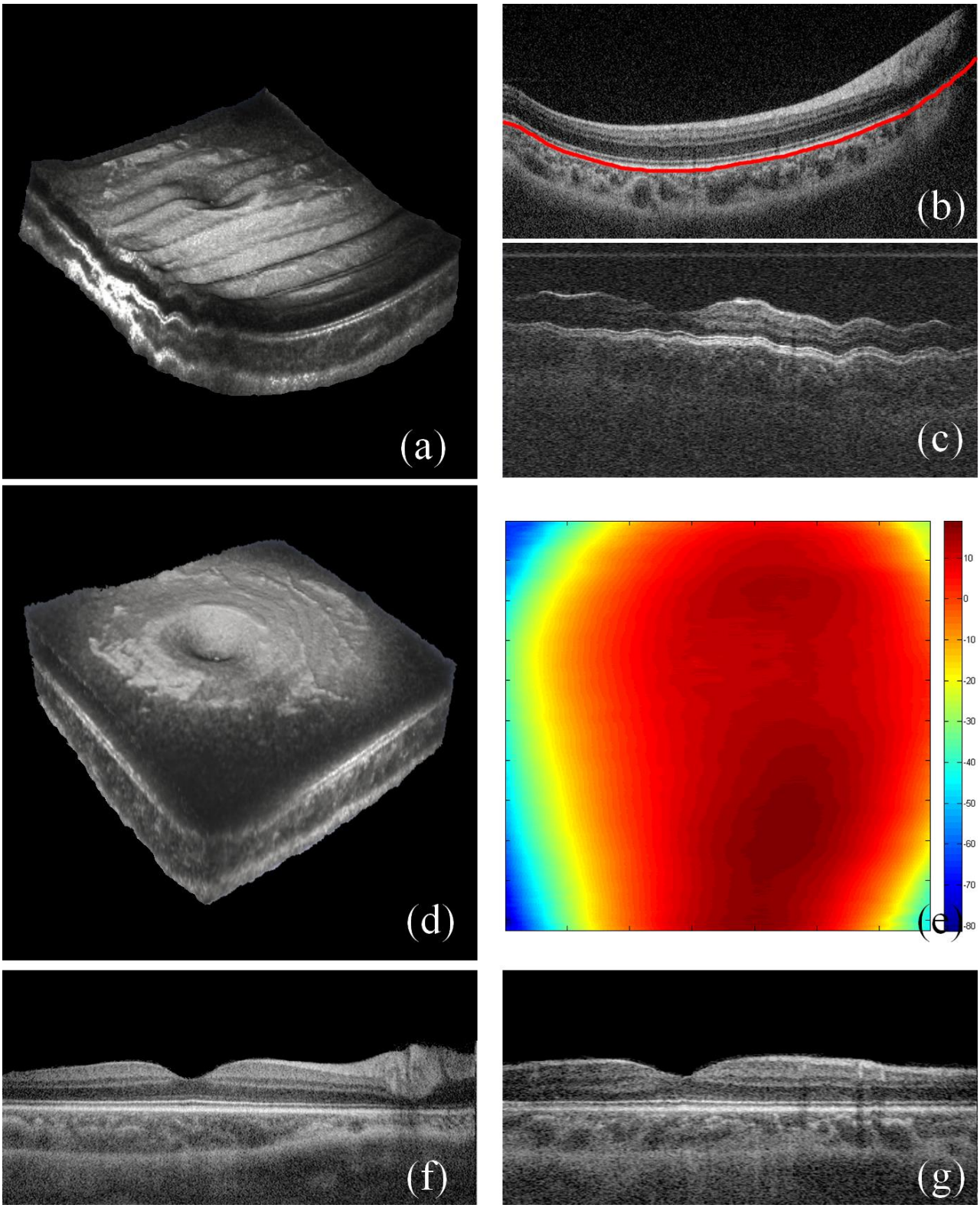

Fig. 3. Retina curvature and movement compensation for 3D volume data. (a) typical 3D volume data acquired by the SD-OCT; (b) typical B-scan with red line marked as RPE layer; (c) typical C-scan without preprocessing; (d) typical

3D volume data after compensation; (e) typical retina curvature map; (f) typical B-scan after curvature compensation; (g) typical C-scan after both movement compensation and curvature compensation.

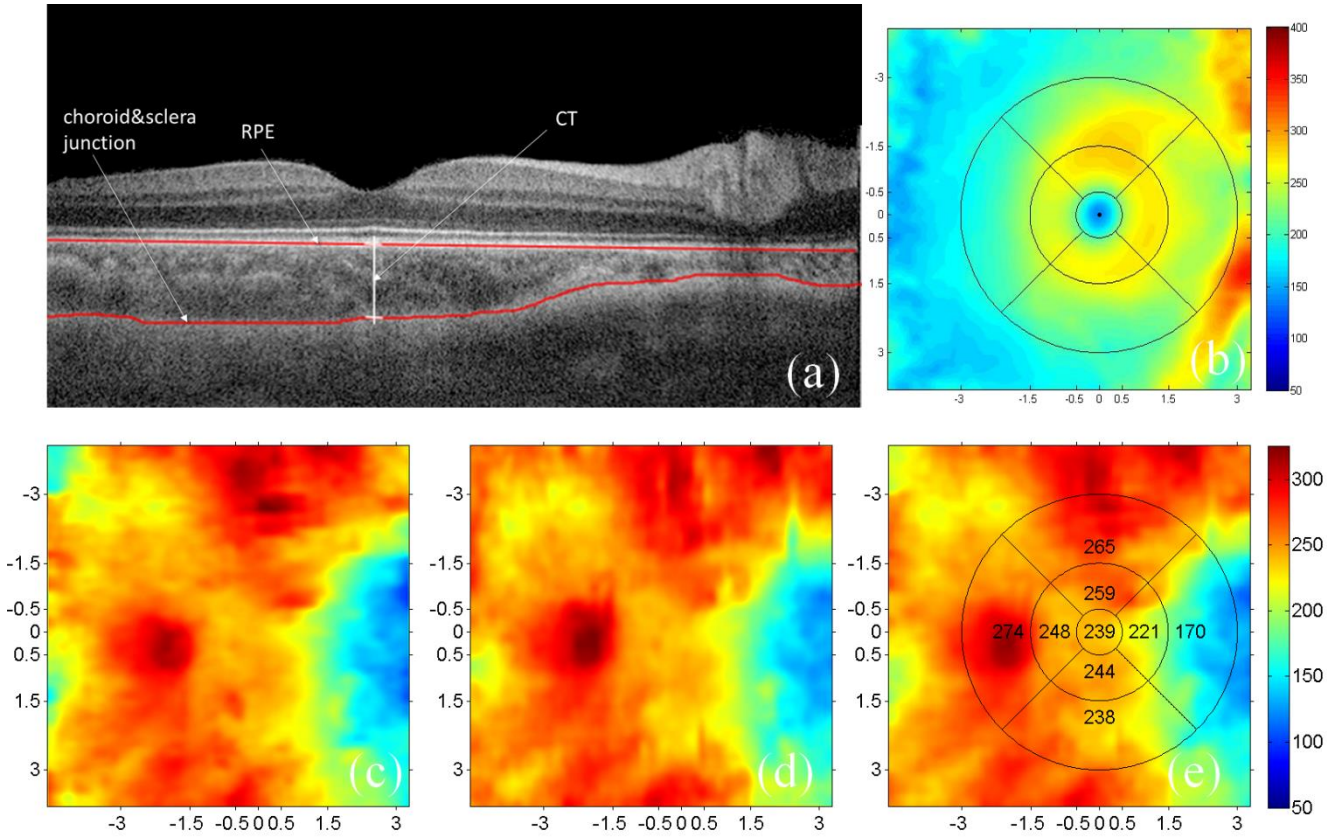

Fig.4. Choroidal thickness measurement and choroidal topographic maps after flattening 3D volume. (a) choroidal thickness are measured by the vertical distance between RPE and choroid & sclera junction(OD); (b) retinal topographic map to determine the position of center of the fovea; (c) choroidal topographic map along B-scan direction; (d) choroidal topographic map along C-scan direction; (e) averaged choroidal topographic map.

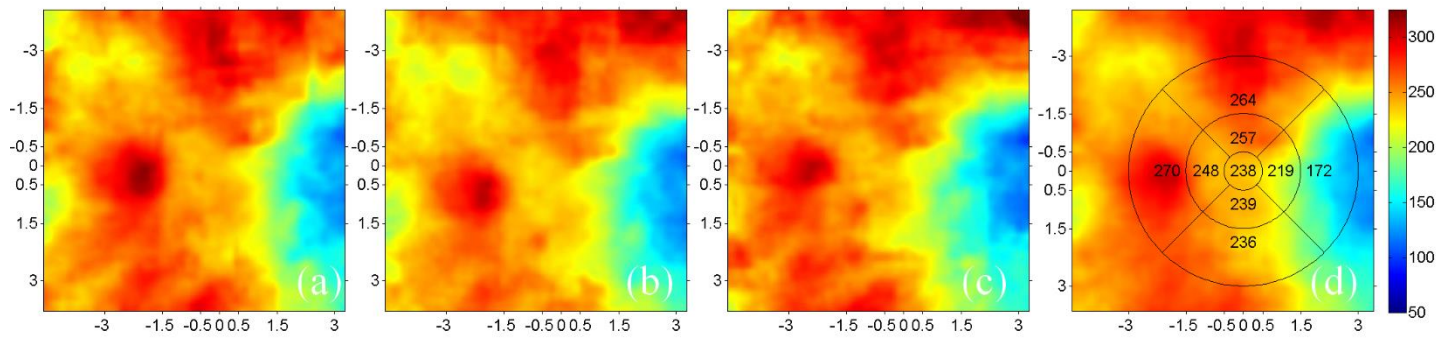

Fig.5. Choroidal topographic maps. (a) choroidal topographic map of eye 1 scan 1, after B-scan based map and C-scan based map averaging; (b) choroidal topographic map of eye 1 scan 2, after B-scan based map and C-scan based map averaging; (c) choroidal topographic map of eye 1 scan3, after B-scan based map and C-scan based map averaging; (d) choroidal topographic map of eye 1 after spatially averaging of all scans.

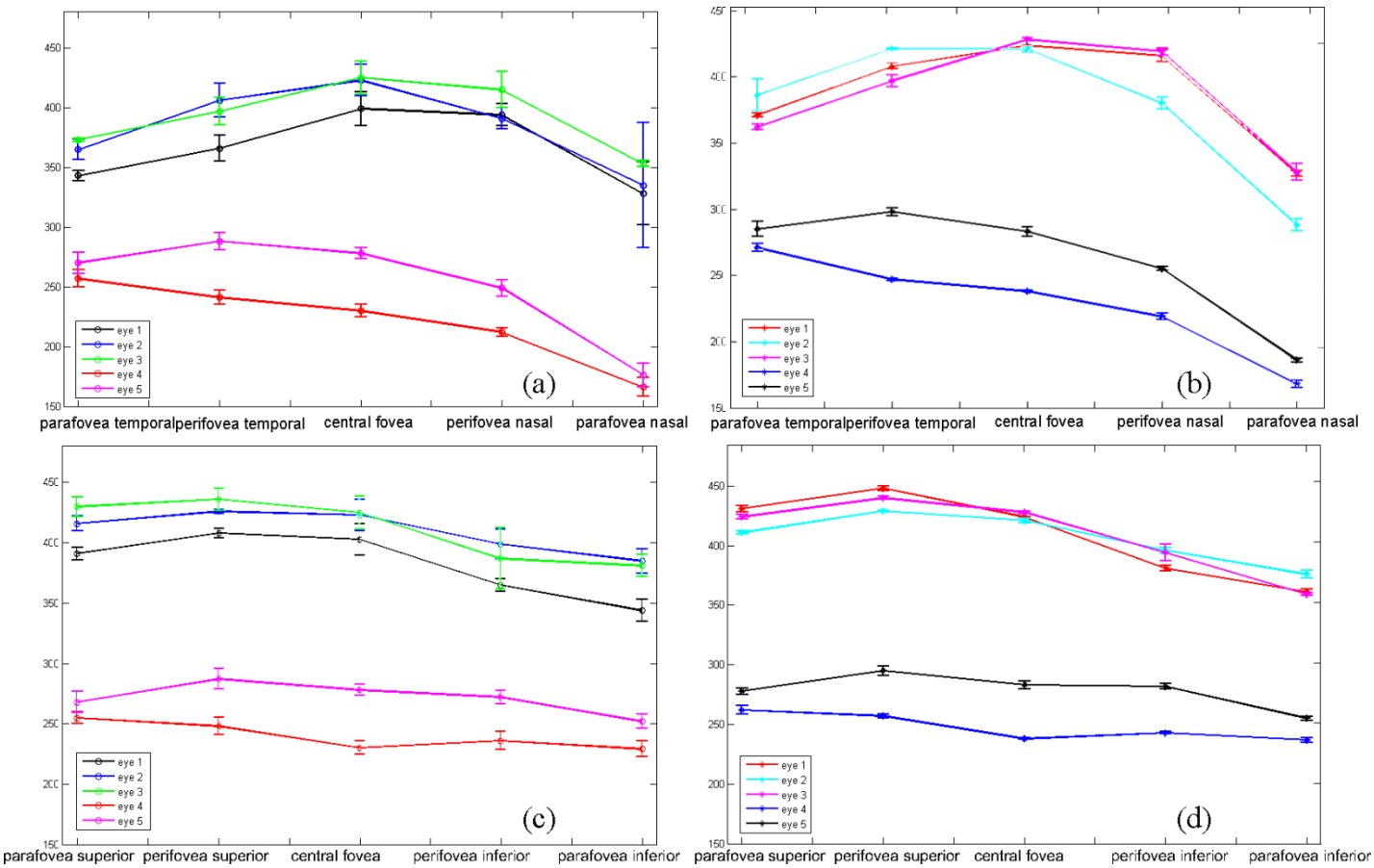

Fig.6. Choroidal thickness measurements from choroidal topographic maps. (a) choroidal thickness in nasal-temporal direction for 5 eyes without preprocessing; (b) choroidal thickness in nasal-temporal direction for 5 eyes with preprocessing; (c) choroidal thickness in superior-inferior direction for 5 eyes without preprocessing; (d) choroidal thickness in superior-inferior direction for 5 eyes with preprocessing.